Energy 327 (2025) 136352

Contents lists available at ScienceDirect

Energy

journal homepage: www.elsevier.com/locate/energy

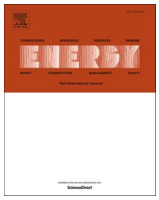

Experimental and DFT investigation on the impact of red mud waste on syngas and char from lignite partial gasification

Bin Zhang [1], Zhihua Tian [1], Qinhui Wang [*], Ruiqing Jia, Dong Ma, Xie Guilin

State Key Laboratory of Clean Energy Utilization, Zhejiang University, Hangzhou, 310027, PR China

ARTICLE INFO

Keywords:
Coal partial gasification
Red mud
Catalytic gasification
Quantum chemical calculation

ABSTRACT

In this study, partial gasification experiments of Shaerhu coal (SC) were conducted under varying temperatures and RM addition ratios, combined with DFT calculations and characterization techniques, to investigate their effects on the properties of products. The results showed that elevated temperatures promoted CO and H_2 generation, whereas RM primarily enhanced H_2 production. Consequently, CGC yields increased by 416.49 mL/g and 47.93 mL/g under temperature rise and RM addition, respectively. Temperature elevation facilitated char graphitization and lateral growth, with oxygen-containing groups initially decreasing and then increasing. RM addition caused an initial increase in oxygenated groups due to enhanced surface reactivity, followed by their consumption and later regeneration. DFT calculations revealed that α-Fe_2O_3, the active component in RM, formed Fe-O-C coordination bonds with SC and acted as a bridge to adsorb O_2, reducing the adsorption energy from −0.32 eV to −0.54 eV and lowering the activation energy. This promoted the cleavage of aromatic structures and regeneration of oxygen-containing groups, explaining their N-shaped variation with RM. The pore structure of char showed a rise-then-fall trend with both temperature and RM, while reactivity declined with temperature but also exhibited an N-type trend with RM, indicating reactivity was primarily governed by chemical structure rather than physical porosity.

1. Introduction

In 2023, global carbon emissions from the utilization of coal and other energy sources exceeded 35 billion tons of carbon dioxide equivalent [1]. Lignite, accounting for approximately 45 % of the world's coal reserves [2], is one of the most abundant coal resources worldwide [3]. Due to its high volatile content and strong gasification reactivity, lignite is considered an ideal feedstock for gasification processes [4]. However, lignite gasification is often associated with substantial CO_2 emissions. Addressing this challenge requires the development of efficient and clean lignite gasification technologies to mitigate CO_2 pollution, which has significant implications for the coal industry and global energy transitions [3].

The reaction temperature of conventional coal gasification typically ranges from 1000 °C to 1700 °C [5], leading to high energy consumption and significant CO_2 emissions. Partial coal gasification [6,7] which utilizes an oxidant to partially combust coal, can generate heat to support the gasification process itself. This approach eliminates the need for high-purity gasification agents or continuous external heat sources, avoids excessively high carbon conversion rates, and significantly reduces both energy consumption and CO_2 emissions [8]. Catalytic gasification technology significantly enhances the gasification reaction rate while reducing the reaction temperature [9,10], thus contributing to lower operational costs and improving industrial feasibility. Integrating this approach with partial gasification offers an efficient pathway for the utilization of lignite resources.

In catalyst selection, alkali metals, alkaline earth metals, and transition metals are among the most commonly used catalyst types [11,12]. Demirbas et al. [14] utilized Na_2CO_3 and K_2CO_3 as catalysts for hydrogen production from olive tree bark and waste tea leaves, finding

* Corresponding author.
E-mail address: qhwang@zju.edu.cn (Q. Wang).
[1] These authors contributed equally to this work.

https://doi.org/10.1016/j.energy.2025.136352
Received 27 February 2025; Received in revised form 9 April 2025; Accepted 27 April 2025
Available online 5 May 2025

that alkali metal salts effectively lowered the activation energy of macromolecular pyrolysis and promoted carbon chain cleavage. Further studies [13] revealed that metals such as Na and K exhibit synergistic effects in enhancing coal char pyrolysis and promoting carbon conversion. Lin et al. [12] found that calcium acetate could reduce the initial reaction temperature of lignite char CO_2 gasification. Their detailed investigation indicated that organically bound Ca^{2+} altered the electronic distribution of aromatic macromolecules in coal char, facilitating C-C bond cleavage. Feng et al. [14] demonstrated that Fe_2O_3 and other Fe-based additives, similar to alkali metal catalysts, exhibit catalytic effects on tar during pyrolysis. Min et al. [15] employed ilmenite as a catalyst for the steam reforming of volatiles (tar) during biomass pyrolysis, attributing its catalytic property to the highly dispersed iron-containing species that effectively convert tar into gases. Yu et al. [16] observed that Fe_2O_3 outperforms KCl and CaO in reducing the activation energy required for the pyrolysis of Huangling coal. Shi et al. [17] reported that the additive modified by Fe_2O_3 surpassed those modified with $MoSi_2$ in catalytic performance. While alkali metal catalysts often demonstrated superior catalytic efficiency compared to Fe-based transition metal catalysts [18], they were prone to volatilization, sintering, and deactivation during high-temperature gasification [19,20]. Transition metal catalysts also faced challenges such as carbon deposition [5] at elevated temperatures. Meanwhile, given the practical constraints of cost-effectiveness, industrial applications require more sustainable and economically viable catalysts to optimize gasification performance. Composite or modified catalysts could combine the advantages of various types but were relatively costly. Consequently, natural mineral catalysts and certain industrial wastes have become preferred options for coal gasification due to their low cost, availability, and catalytic efficiency [21]. Bayer-process red mud (RM), a solid waste generated during aluminum production, was a promising candidate as a catalyst [22]. With global RM reserves exceeding 2.7 billion tons [23], its disposal posed significant environmental challenges. RM primarily comprised catalytically active components such as Fe_2O_3, Al_2O_3, Na_2O, and CaO [24]. Studies suggested that the catalytic activity of RM was mainly attributed to Fe_2O_3, with its unique solid-solution structure providing abundant active lattice oxygen sites [25]. Compared to single Fe-based catalysts, RM exhibited superior resistance to carbon deposition, better catalytic performance, and lower cost. Li et al. [23] reported that RM functioned as a fluxing agent to reduce coal ash melting temperatures. Wang et al. [21] highlighted the strong regulatory effect of RM on tar composition. Li and Chang et al. [26] showed that RM could increase carbon conversion in char gasification, thereby improving gasification efficiency. Lee et al. [27] investigated the desulfurization performance of Fe_2O_3 in RM using a combination of DFT calculations and experiments. Their findings indicated that Fe_2O_3 facilitated COS removal while generating value-added CO. Similarly, Huang et al. [28] employed DFT calculations to study the adsorption of benzene rings on hematite, a common RM component, and elucidated the most probable adsorption configurations and C–C bond cleavage pathways. Overall, RM represents a viable alternative to Fe_2O_3 and other single Fe-based catalysts for coal gasification, offering economic and environmental advantages. This shift toward waste-derived catalysts not only improves the cost-effectiveness of coal gasification but also promotes the circular economy and industrial waste valorization.

Previous research has demonstrated that RM can lower reaction temperatures, accelerate reaction rates, and alter product distributions. However, most studies have focused on CO_2 and steam gasification or pyrolysis, with an emphasis on the catalytic effects of RM on syngas and tar characteristics. Research on the partial gasification of lignite in an air atmosphere is limited, especially concerning the impact of RM on the properties of partially gasified char. Additionally, the catalytic pathways through which RM influences char structure during gasification remain largely unexplored. This study aims to address these gaps by investigating the effects of temperature and RM additives on the characteristics of syngas and char during lignite partial gasification. Experiments were conducted in a self-designed fluidized bed reactor using air as the gasifying agent under low-temperature conditions. To elucidate the mechanisms by which temperature and RM influence lignite partial gasification, characterization techniques including XRD, Raman spectroscopy, XPS, and FTIR were employed, complemented by DFT calculations. The findings of this study provide theoretical guidance into the efficient and clean utilization of lignite and RM, contributing to cost and energy input reduction while enabling the valorization of RM waste for environmental protection.

2. Materials and methods

2.1. Materials

The coal sample used in this study was Sharhu coal (SC) from Xinjiang, China, a lignite with high volatile content. After crushing and sieving, coal particles with a size range of 0.9–2 mm were selected as the experimental material. Before the experiments, the coal samples were dried in an oven at 105 °C for 6 h to remove moisture. Proximate and ultimate analyses of the coal samples were performed based on standards GB/T 212–2008 and GB/T 476–2015, respectively, with the results presented in Table 1.

The red mud (RM) used in the experiments was obtained from an aluminum production facility. The RM was dried in an oven at 105 °C for 6 h to remove moisture, followed by sieving to achieve a particle size range of 0.1–0.2 mm to facilitate separation. The chemical composition of the RM was analyzed using X-ray fluorescence (XRF, Bruker S8 Tiger, Germany) spectroscopy with a Rh-target X-ray tube (50 kV, 40 mA). The main components of RM include Fe_2O_3、Al_2O_3、SiO_2、TiO_2 and Na_2O, with their specific contents detailed in Table 2.

2.2. Experimental method

2.2.1. Experimental system and process

The experiments in this study were conducted using a self-designed bubbling fluidized bed reactor, as illustrated in Fig. 1. The experimental system consists of three main components: a gas system, a reaction system, and a collection and analysis system. The fluidized bed reactor tube is heated using electric heating wires and silicon carbide rods, capable of reaching a maximum temperature of 950 °C, and is insulated with refractory bricks. A preheating section is installed before the fluidized bed to heat the carrier gas to a desired temperature before entering the reactor.

Before conducting the partial gasification experiments, the system was tested for airtightness using a soap solution to ensure a sealed setup. The fluidized bed was preheated to 650 °C using a computer-controlled heating program. Each experiment used 30 g of coal, with a feed coal flow rate of 0.289 kg/h. Based on prior research [29], an air equivalence ratio (ER) of 0.1 was found to yield optimal production, so the air flow rate was set to 3.18 L/min to maintain this ER according to Eq. (1). The flow rate of N_2 mixed in was 1.22 L/min, making the total gas flow rate 4.4 L/min to ensure that the bed material could reach a fluidized state and was not blown out. To investigate the effects of temperature and RM addition ratio on product characteristics, various preheating temperatures and RM addition ratio were tested, as shown in Table 3. Each reaction lasted approximately 8 min. A Fourier-transform infrared gas analyzer (GASMET DX4000, Finland) was used to monitor syngas composition, including CO_2 and CO. Once the reaction stabilized, gas

Table 1
Proximate, ultimate and calorific value analysis of coal.

Sample	Proximate analysis (ad, wt%)				Ultimate analysis (ad, wt%)					LHV (MJ/kg)
	M	A	V	FC	C	H	N	S_t	O_{diff}	
SC	5.04	5.66	43.60	45.70	66.27	5.12	1.01	0.35	16.55	28.33

Note: (1) M: Moisture, A: Ash, V: Volatile, FC: Fixed carbon; (2) ad: Air dry basis, t: Total, diff: By difference.

Table 2
XRF analysis data of RM.

Chemical components	Fe_2O_3	Al_2O_3	SiO_2	Na_2O	TiO_2	CaO
Content (%)	35.73	24.7	18.33	14.09	4.93	2.22

products were collected for 2 min. The char and RM residues were cooled and collected through the hopper. After separation based on particle size, the samples were subjected to characterization tests. Each experiment was repeated three times to minimize experimental error.

$$ER = \frac{(m_{air}/m_{coal})_{exp}}{(m_{air}/m_{coal})_{stoic}} = \frac{V_{air}}{V_{coal}\cdot\left[0.0889\cdot(C_{ad}+0.375S_{ad})+0.265\cdot\left(H_{ad}-\frac{O_{ad}}{8}\right)\right]} \quad (1)$$

where ER represents the air equivalence ratio which is defined as the ratio of the air supplied under experimental conditions to the air required under stoichiometric conditions; V_{coal} (g /min) represents the coal feeding rate; V_{air} (L/min) represents the air supply rate.

2.2.2. Calculation of gasification index

(1) The yield of partial gasification product

The yields of char, liquid and syngas were calculated according to Eqs. (2)–(4):

$$Y_{char} = \frac{m_{char}}{m_{coal}}\cdot 100\% \quad (2)$$

$$Y_{liquid} = \frac{m_{liquid}}{m_{coal}}\cdot 100\% = \frac{m_2 - m_1}{m_{coal}}\cdot 100\% \quad (3)$$

$$Y_{gas} = \left(1 - Y_{liquid} - Y_{char}\right)\cdot 100\% \quad (4)$$

where Y_{char}, Y_{liquid}, Y_{gas} (%) represent the yields of char, liquid products and syngas generated by coal partial gasification, respectively; m_{char}, m_{liquid}, m_{coal} (g) represent the mass of char, liquid products and coal, respectively; m_2 and m_1 (g) represent the mass of the tar condensation unit after and before the reaction.

(2) Syngas lower heating value and gasification efficiency

The lower heating value of syngas (LHV_{gas}) was calculated according to Eq. (5):

$$LHV_{gas} = \sum V_i LHV_i \quad (5)$$

where LHV_{gas} (MJ/Nm^3) represents the lower heating value of syngas; V_i (%) represents the volume fraction of various combustible gases in syngas; LHV_i represents the lower heating value of various combustible gases, as shown in Table 4.

The gasification efficiency is defined as the ratio of the chemical energy of the syngas produced by the gasification reaction to the chemical energy of the raw coal, calculated according to Eq. (6):

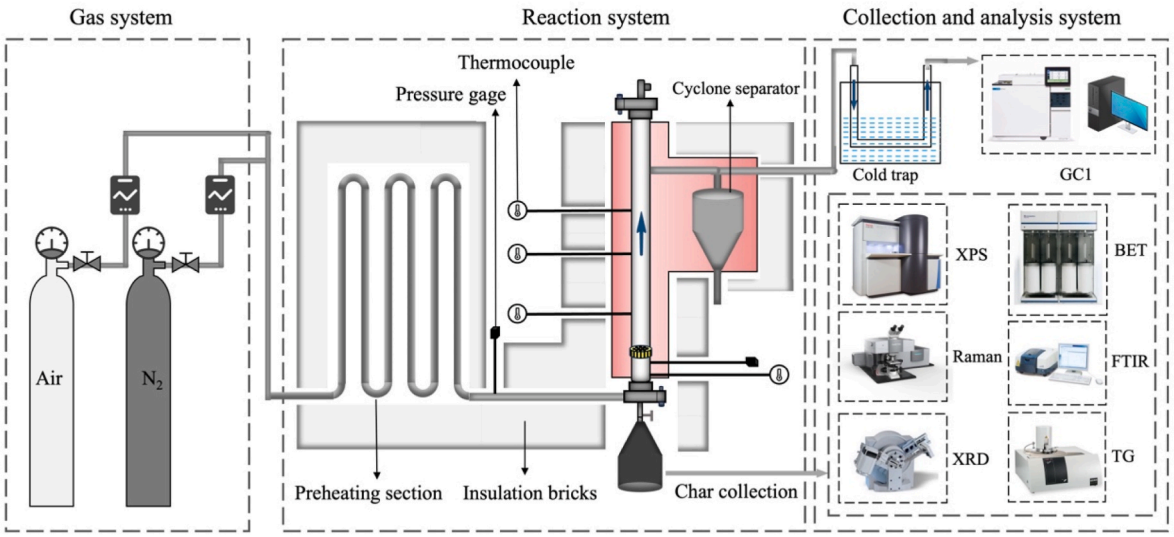

Fig. 1. Schematic diagram of fluidized bed reactor system.

Table 3
Experimental parameter settings.

Case	Sample	Preheating temperature (°C)	RM addition ratio (%)
1	SC	600	0
2	SC	650	0
3	SC	700	0
4	SC	750	0
5	SC	800	0
6	SC + RM	700	5
7	SC + RM	700	10
8	SC + RM	700	15
9	SC + RM	700	20
10	SC + RM	700	25
11	SC + RM	700	30

Table 4
The lower heating value of commonly used combustible gases.

Gas	H_2	CO	CH_4	C_2H_4	C_2H_6	C_3H_6	C_3H_8
LHV (MJ/Nm^3)	10.79	12.64	35.88	59.44	64.35	87.61	93.18

$$\eta = \frac{V_{gas} \cdot LHV_{gas}}{M_{coal} \cdot LHV_{coal}} \cdot 100\% \tag{6}$$

where η (%) represents the gasification efficiency; LHV_{coal} (MJ/kg) represents the lower heating value of the raw coal.

(3) Syngas flow rate and syngas conversion rate

The flow rate of syngas can be calculated based on the volume content of nitrogen in the syngas, as shown in Eq. (7):

$$V_{gas} = \frac{100 \cdot V_{N2}}{X_{N2}} \tag{7}$$

where V_{gas} (L/min) represents the flow rate of the syngas; V_{N2} (L/min) represents the flow rate of nitrogen in the input gas; X_{N2} (%) represents the volume fraction of nitrogen in the syngas.

Once the reaction stabilized, gas products were collected for 2 min. The syngas conversion rate during the partial gasification process is defined as the ratio of the carbon content in the syngas to the carbon content in the coal, as shown in Eq. (8):

$$\alpha_C = \frac{V_{gas} \cdot C_{gas}}{V_{coal} \cdot C_{ad}} \cdot 100 = \frac{V_{gas} \sum \frac{X_n}{22.4} \cdot 12}{V_{coal} \cdot C_{ad}} \cdot 100\% \tag{8}$$

where α_C (%) represents the syngas conversion rate; V_{gas} (L/min) represents the flow rate of gasified syngas; X_n (%) represents the volume fraction of 1 times CO, CO_2, CH_4, 2 times C_2H_4 and C_2H_6, and 3 times C_3H_6 and C_3H_8 in the syngas; V_{coal} (g/min) represents the coal feeding rate; C_{ad} (%) represents the carbon content of the coal; C_{gas} (%) represents to the carbon content of the syngas.

2.3. Product and catalysts characterization

The main components of the syngas (CO, CO_2, CH_4, H_2 and C_1-C_3 alkanes) were quantified using a gas chromatograph (GC, Agilent 8860, USA). The organic functional groups of the char were characterized using Fourier-transform infrared spectroscopy (FTIR, Thermo Scientific Nicolet iS20, USA) with potassium bromide (KBr) pellet preparation in the 400-4000 cm^{-1} wavenumber range. The results were further verified by X-ray photoelectron spectroscopy (XPS, Thermo Scientific K-Alpha, USA) using monochromatic Al Kα radiation (hv = 1486.6 eV). Raman spectroscopy (Raman, Horiba LabRAM HR Evolution, Japan) was used to analyze the internal crystallinity and order of the char in the 800-1800 cm^{-1} spectral range. X-ray diffraction (XRD, Rigaku SmartLab SE, Japan) was performed using Ni-filtered Cu Kα radiation, with a 2θ range of 10°–80° and a scan rate of 2°/min, to further characterize the crystallinity of the char. The pore characteristics of the char were determined using the N_2 adsorption method on a fully automatic surface area and porosity analyzer (Micromeritics ASAP 2460, USA), with a degassing temperature of 300 °C and a degassing time of 7 h. The combustion reactivity of the char was tested using a simultaneous thermal analyzer (Mettler TGA/DSC 3+, Switzerland).

2.4. Simulation method

We have employed the Vienna Ab Initio Package (VASP) [30,31] to perform all the spin-polarized density functional theory (DFT) calculations within the generalized gradient approximation (GGA) in the PBE [32] formulation. We have chosen the projected augmented wave (PAW) potentials [33,34]to describe the ionic cores and take valence electrons into account using a plane wave basis set with a kinetic energy cutoff of 500 eV. Partial occupancies of the Kohn−Sham orbitals were allowed using the Methfessel-Paxton smearing method and a width of 0.05 eV. The electronic energy was considered self-consistent when the energy change was smaller than 10-5 eV. A geometry optimization was considered convergent when the residual forces were smaller than 0.03 eV/Å. Finally, the adsorption energies (E_{ads}) were calculated as Eq. (9):

$$E_{ads} = E_{total} - E_{sub1} - E_{sub2} \tag{9}$$

where E_{total} is the total energies of the binding structure, kJ/mol; E_{sub1} and E_{sub2} are the two independent parts within the composite structure, kJ/mol. The Gibbs free energy of a gas phase molecule or an adsorbate on the surface was calculated by Eq. (10)

$$G = E + ZPE - TS \tag{10}$$

where E (kJ/mol) is the total energy; ZPE (kJ/mol) is the zero-point energy; T is the temperature in kelvin, 298.15 K; S (kJ/(mol·K)) is the entropy; Finally, transition states for elementary reaction steps were determined by a combination of the nudged elastic band (NEB) method and the dimer method. In the NEB method, the path between the reactant and product is discretized into a series of structural images. The image that is closest to a likely transition state structure was then employed as an initial guess structure for the dimer method.

3. Results and discussion

3.1. Effects of temperature and RM additives on gasification performance

3.1.1. Product distribution and gasification index

Fig. 2 illustrates the product distribution and gasification indexes of SC under various experimental conditions. Fig. 2(a) shows that, at a constant ER, temperature significantly influences the product distribution during partial gasification. As the temperature increases, further gasification and macromolecular cracking are promoted, increasing syngas yield from 16.45 % to 30.46 %, with the yield of char and liquid products decreasing from 70.2 % to 60.2 % and from 13.35 % to 9.33 %, respectively. This phenomenon can be attributed to intensified heat and mass transfer at higher temperatures, which accelerates both the cracking process and the release of volatile components, as well as the participation of more fixed carbon in the gasification reactions. Additionally, as shown in reactions **R1-R7** [12,35], elevated temperatures enhance the Boudouard reaction, water-gas shift reaction (WGSR), complete and incomplete combustion of carbon, leading to greater gas production. The increased reaction rates intensify the gasification process and promote a more severe secondary reaction of the macromolecular structures in the char, leading to higher gas production [36].

$$C + CO_2 \rightarrow 2CO, Endothermic \quad \text{R1}$$

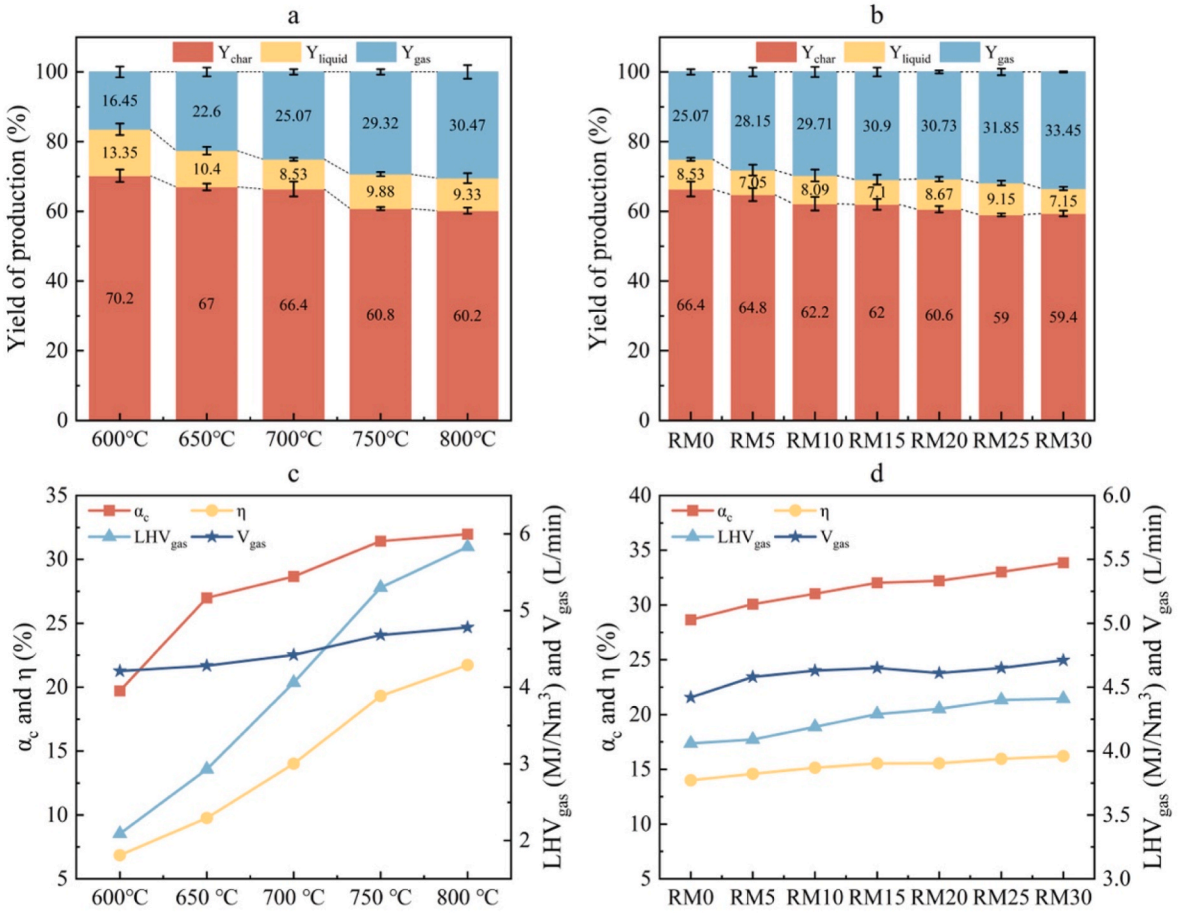

Fig. 2. Product distribution and gasification indexes at different temperatures (a, c) and RM addition ratios (b, d).

$$CO + H_2O \rightarrow H_2 + CO_2, Exothermic \quad \text{R2}$$

$$C + 0.5O_2 \rightarrow CO, Exothermic \quad \text{R3}$$

$$C + O_2 \rightarrow CO_2, Exothermic \quad \text{R4}$$

$$C + 2H_2 \rightarrow CH_4, Exothermic \quad \text{R5}$$

$$CH_4 + 2H_2O \rightarrow CO_2 + 4H_2, Endothermic \quad \text{R6}$$

$$CH_4 + CO_2 \rightarrow 2CO + 2H_2, Endothermic \quad \text{R7}$$

Fig. 2(b) illustrates that, at a constant gasification temperature, the addition of RM increases syngas yield and decreases char and liquid product yields. As the RM addition ratio rises from 5 % to 30 %, its catalytic effect becomes more pronounced, reducing char yield by 1.6 %–7.4 % and increasing syngas yield by 0.51 %–5.07 %. These findings are consistent with those of Wang et al. [21]. On one hand, the presence of solid additives affects heat and mass transfer during gasification [37, 38], potentially altering the migration paths of radicals in the process. On the other hand, RM serves as a catalyst that accelerates the gasification reaction and increases the reaction rate. As noted by Zhou et al. [25], the primary catalytic component in RM is Fe_2O_3, which participates in a series of reactions with the carbon in coal, as shown in reactions **R8-R11**. The presence of RM facilitates greater carbon participation in these reactions, leading to a reduction in char yield and an increase in syngas production. Moreover, the unique structure of RM provides additional active sites [5], further promoting the reaction. This not only enhances coal conversion but may also result in the secondary cracking of tar, thereby decreasing the liquid product yield.

$$3Fe_2O_3(s) + C(s) \rightarrow 2Fe_3O_4(s) + CO(g) \quad \text{R8}$$

$$Fe_3O_4(s) + C(s) \rightarrow 3FeO(s) + CO(g) \quad \text{R9}$$

$$FeO(s) + C(s) \rightarrow Fe(s) + CO(g) \quad \text{R10}$$

$$Fe_2O_3(s) + 3C(s) \rightarrow 2Fe(s) + 3CO(g) \quad \text{R11}$$

The results in Fig. 2(c) and (d) demonstrate that gasification efficiency (η), lower heating value of syngas (LHV_{gas}), and gas conversion rate (α_C) exhibit high sensitivity to temperature increase. As the temperature rises, η, LHV_{gas}, and α_C increases continuously, with improvements of 14.90 %, 3.74 MJ/Nm^3, and 14.02 %, respectively. This can be attributed to the enhanced release of volatile matter in coal and the intensification of gas-solid and gas-gas reactions (**R1-R7**) which raise the combustible gas components (CGC) such as H_2, CO, and CH_4 in the syngas. Although RM also contributes to improvements in gasification indexes, its effect is relatively less significant, with LHV_{gas} reaching 4.36 MJ/Nm^3 at an RM addition ratio of 25 %. This is likely because key reactions in coal gasification, such as the Boudouard reaction, typically require elevated temperatures to proceed effectively. Both temperature and RM addition increase syngas flow, with the maximum flow reaching 4.78 L/min at higher temperatures and 4.71 L/min at 30 % RM addition. These results suggest that RM has a limited catalytic effect on gasification efficiency compared to the temperature increase.

3.1.2. Gas composition

Fig. 3 shows the gas composition under different experimental conditions, which primarily consists of CO, CO_2, H_2, and C_1-C_3 alkanes. During coal thermal reactions, these non-condensable light gases are

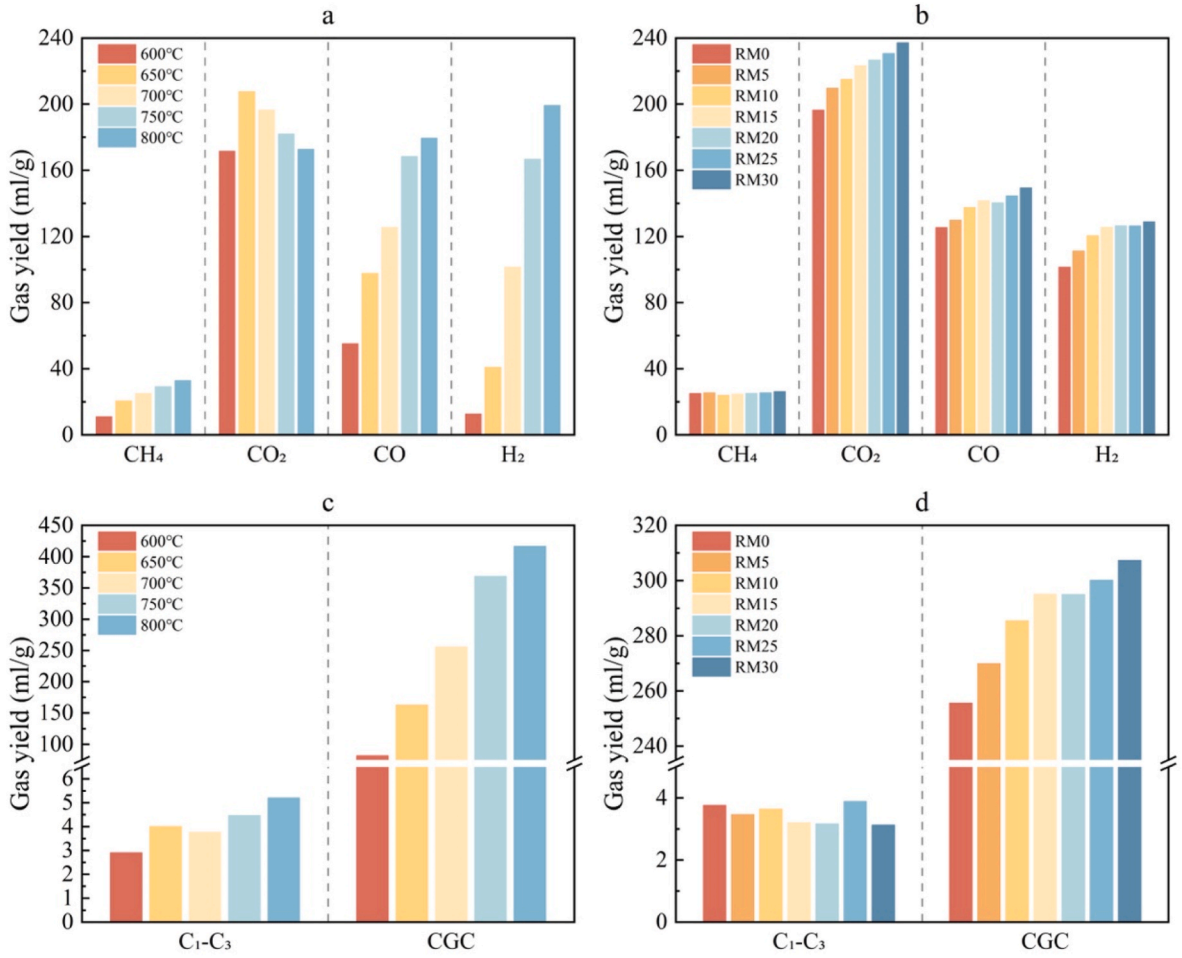

Fig. 3. Gas composition at different temperatures (a) and RM addition ratios (b).

mainly generated through the thermal cracking and oxidation of macromolecular structures and functional groups in coal [39]. CO and CO_2 are produced through the thermal decomposition of oxygen-containing groups and carbon oxidation [40] while H_2 generally arises from reactions such as aliphatic hydrocarbon cyclization, WGSR, and methane reforming(**R2**, **R6**, and **R7**) [21]. C_1-C_3 alkanes are formed through cleavage and hydrogenation of aliphatic side chains [41]. The composition of syngas is influenced by these processes, with further interconversion among different gas species occurring at higher temperatures.

As shown in Fig. 3, CGC yield increases significantly as temperature increases, rising from 81.68 ml/g to 416.49 ml/g. CO and H_2 are the major contributors, rising by 124.24 ml/g and 186.52 ml/g, respectively. At 600 °C, the yield of H_2 is relatively low at 12.62 ml/g, reflecting insufficient energy for endothermic reactions, such as the Boudouard reaction and methane reforming, which render CO_2 relatively inert at low temperatures [42]. At elevated temperatures, the accelerated decomposition of macromolecular structures in coal promotes the release of more alkanes and enhances the production of H_2 and CO. The increase in CGC yield leads to higher gasification efficiency. Studies show that excess lattice oxygen at high temperatures leads to over-oxidation of CO to CO_2 [5], but rising temperature can increase the consumption of CO_2 and generate CO through the Boudouard reaction, thereby enhancing gasification performance [43]. Consequently, CO_2 yield exhibits a rise-and-fall trend, peaking at 225.73 ml/g at 650 °C.

With increased RM addition, CGC yield rises, peaking at 47.93 ml/g. Among the CGC, H_2 shows the greatest increase, with a yield increase of 27.39 ml/g, corresponding to a growth rate of 26.99 %. This enhancement can be attributed to two main factors. First, the unpaired electrons and unoccupied molecular orbitals of the Fe species in the Fe-based catalyst may induce the cleavage of covalent bonds in the coal, thereby promoting radical generation and the release of small-molecule gases [44]. Additionally, the metal oxides in RM exhibit catalytic activity [45], promoting aromatic ring condensation to produce H_2. Second, as a reductive gas, H_2 reacts with Fe_2O_3 in RM (**R12-R15**) [46], further enhancing H_2 generation. In contrast, RM has little effect on CH_4 and C_2-C_3 alkanes, which have the highest LHV_{gas} among the CGC, leading to limited changes in LHV_{gas} despite RM addition. The yields of CO and CO_2 also increase with RM addition, reaching maximum increments of 24.89 ml/g and 40.77 ml/g, respectively. Fe_2O_3 in RM reacts with carbon in char through carbothermal reactions (**R8-R11**) and reduction reactions with CO (**R16-R19**) [47], promoting CO and CO_2 production. However, when RM exceeds 15 %, the growth rates of CO_2 and CO plateau, indicating the catalytic effect of RM approaches saturation. Notably, the addition of RM demonstrates a dual effect on syngas production characteristics. Compared to the maximum increase in CO_2 yield of 40.77 ml/g, the CGC yield increased by 47.93 ml/g, thereby enhancing the LHV_{gas} of the gas. This indicates that although the addition of RM promotes CO_2 generation through enhanced gasification reactions, its enhancement effect on syngas quality is more pronounced. Crucially, achieving equivalent CGC enhancement through thermal means would require elevated reaction temperatures, which in industrial applications necessitates increasing the air equivalence ratio. However, our previous study [29] reveals that an increase in the air equivalence ratio shifts the dominant reaction in SC partial gasification from pyrolysis to gasification. This transition amplifies a higher CO_2

yield and a lower char yield, with the increase in CO_2 yield significantly exceeding the reduction in CGC yield. Consequently, under equivalent syngas quality, RM addition effectively reduces the activation energy required for SC partial gasification, thereby indirectly lowering the reaction temperature. In this indirect way, CO_2 emissions can be reduced while simultaneously increasing char yield and enhancing syngas quality.

$$3Fe_2O_3(s) + H_2(g) \rightarrow 2Fe_3O_4(s) + H_2O(g) \quad \text{R12}$$

$$Fe_3O_4(s) + H_2(g) \rightarrow 3FeO(s) + H_2O(g) \quad \text{R13}$$

$$FeO(s) + H_2(g) \rightarrow Fe(s) + H_2O(g) \quad \text{R14}$$

$$Fe_2O_3(s) + 3H_2(g) \rightarrow 2Fe(s) + 3H_2O(g) \quad \text{R15}$$

$$3Fe_2O_3(s) + CO(g) \rightarrow 2Fe_3O_4(s) + CO_2(g) \quad \text{R16}$$

$$Fe_3O_4(s) + CO(g) \rightarrow 3FeO(s) + CO_2(g) \quad \text{R17}$$

$$FeO(s) + CO(g) \rightarrow Fe(s) + CO_2(g) \quad \text{R18}$$

$$Fe_2O_3(s) + 3CO(g) \rightarrow 2Fe(s) + CO_2(g) \quad \text{R19}$$

3.1.3. Sensitivity analysis

Gray relational analysis (GRA) was implemented to evaluate the sensitivity of temperature and RM addition ratio on four output parameters: char yield, syngas yield, CGC yield, and CO_2 yield, based on our previous study [48]. Since the data results were as large as possible, the data were normalized using the min-max normalization method [49]. The normalized data and the calculated gray relational coefficients (GRC) are presented in Table S1, while the gray relational grade (GRG) values for the two reaction conditions concerning the output parameters are summarized in Table 5. A higher GRG value indicates greater sensitivity of the reaction condition to the experimental outcome. Notably, while both reaction conditions exhibit comparable sensitivity on syngas yield (GRG difference <1 %), a 22.2 % disparity emerged in char yield sensitivity with a GRG of 0.486 for temperature and 0.594 for RM addition. This discrepancy arises from their distinct mechanisms in promoting SC partial gasification. While temperature accelerates the gasification reaction rate, RM addition introduces more active sites and releases extra lattice oxygen, thereby accelerating char consumption. Under fixed air equivalence ratios, the O_2 content available for gasification remains unchanged. Consequently, catalytic decomposition generated by RM (**R8-R11**) demonstrates superior carbon consumption efficiency compared to thermally driven gasification. Similarly, RM addition enhances the reaction rates of **R16-R19**, making CO_2 yield significantly more sensitive to RM addition than temperature. Consistent with previous interpretations, RM primarily catalyzes coal char structural transformations to enhance H_2 generation, whereas temperature elevation primarily drives gasification reactions such as the Boudouard reaction, which boosts CO and H_2 production. However, the sensitivity difference between these two factors is minimal, with both exhibiting high GRG values exceeding 0.84. Moreover, the cost increase associated with temperature elevation is generally much higher than the RM addition, an industrial waste, in coal partial gasification. As described in this study, temperature elevation in practical applications is achieved by increasing the ER, which simultaneously raises CO_2 yield. Consequently, compared to improving temperature, RM catalytic gasification not only repurposes RM waste to mitigate environmental concerns but also can enhance syngas quality at a lower cost.

Table 5
Results of average GRG values.

Phases	Syngas yield	Char yield	CGC yield	CO_2 yield
Temperature	0.858	0.486	0.954	0.508
RM additive ratio	0.866	0.594	0.849	0.91

3.2. Effects of temperature and RM additives on char properties

3.2.1. Carbon structure of char

In highly disordered carbon materials, such as lignite, the first-order Raman spectrum (800-1800 cm^{-1}) is commonly used to analyze the carbon framework structure [50]. In this study, the spectra in this range are deconvoluted into ten Gaussian peaks using *Peakfit V4.12* software [51,52]. Fig. 4 (a) shows the fitting results for char prepared at 700 °C with an RM addition ratio of 0 %, achieving a regression coefficient (R) above 0.99, indicating an excellent fit. The microstructural characteristics of the carbon material are analyzed through the intensity or ratios of characteristic peaks, including the G, G_r, V_L, V_r, D, and S bands [53]. The G band primarily corresponds to aromatic ring vibrations, while the D band is related to C-C bond vibrations in larger aromatic clusters (>6 rings) [54]. The G_r (1540 cm^{-1}), V_L (1465 cm^{-1}), and V_r (1380 cm^{-1}) bands represent small aromatic ring clusters (3–5 rings) typical of amorphous carbon. Detailed peak assignments of the Raman spectra are summarized in Table S2.

In Raman spectra, structural variations in coal may cause significant fluorescence interference [55]. The fluorescence intensity is closely related to the structural characteristics of coal and char. To investigate the relationship between fluorescence intensity and the active components in these materials, the drift coefficient α was defined to quantify fluorescence intensity, as shown in Eq. (11):

$$\alpha = \frac{y_B - y_A}{y_D - y_A} \quad (11)$$

where y_A, y_B, and y_D represent the Raman intensities at 800 cm^{-1}, 1800 cm^{-1}, and 1340 cm^{-1}, respectively. α quantifies the ratio of baseline drift intensity to the Raman intensity within the specified wavebands, as illustrated in Fig. 4 (b).

Fig. 4 (c) and (d) show the variations in Raman characteristic parameters, including A_t, $A_{(Gr + VL + Vr)}/A_D$, A_G/A_D, A_{Gr}/A_D, and α as functions of temperature and RM addition. A_t, defined as the sum of the fitted peak areas, characterizes the degree of disorder in the sample, with higher values reflecting greater disorder. Results indicate that A_t initially decreases and then increases with rising temperature. A_t is influenced by the light absorption of samples, Raman scattering efficiency, and the oxygen-containing components that induce resonance effects [51,52]. Oxygen-containing functional groups and electron-rich structures typically exhibit high Raman scattering efficiency.

Thus, the consumption and transformation of these groups suppress A_t. The observed decrease followed by an increase in A_t suggests that the oxygen-containing functional group content decreases initially and then increases with temperature, corresponding to a reduction followed by an intensification in the degree of structural disorder in the char. At low temperatures, highly reactive oxygen-containing functional groups are preferentially consumed. As the temperature rises, more significant reactions occur, leading to the decomposition of large aromatic rings and the formation of small aromatic rings and oxygen-containing functional groups. Upon introducing RM as a catalyst, A_t increases, indicating that active sites on RM facilitate gasification reactions, generating more oxygen-containing groups. As RM addition increases, A_t initially decreases and then gradually rises, reflecting a similar trend in the content of oxygen-containing groups in the char. At lower RM levels, RM facilitates the decomposition of oxygen-containing groups, enhancing the formation of small molecule gases. With further increases in RM addition, most of the reactive structures in the coal have already reacted with lattice oxygen provided by RM catalysis. RM then interacts with macromolecular structures in the coal, providing additional active sites that catalyze their decomposition, leading to the generation of more oxygen-containing groups and increases the structural disorder of char and A_t. Collectively, these effects produce a characteristic N-shaped

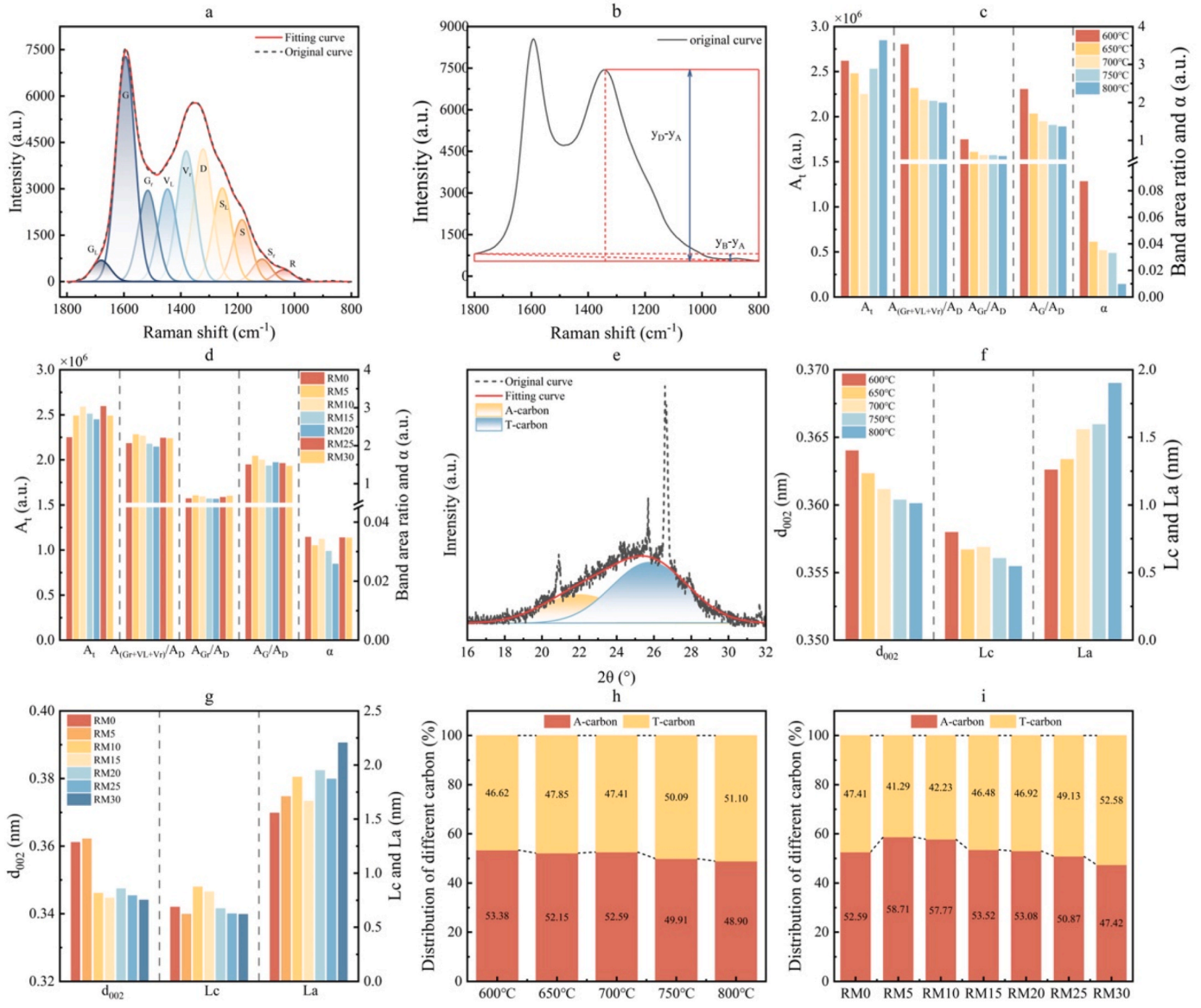

Fig. 4. Raman and XRD analysis of the samples: (a) Raman peak fitting example; (b) drift coefficient example; (c)–(d) Raman parameters of the samples; (e) XRD fitting example; (f)–(g) crystal parameters of the samples; (h)–(i) carbon distribution of the samples.

trend, an initial decrease followed by a subsequent increase in the content of oxygen-containing groups with increasing RM addition.

The ratios of Raman band areas, $A_{(Gr + VL + Vr)}/A_D$ and A_{Gr}/A_D, reflect the relative proportions of small (3–5 rings) to large (>6 rings) aromatic structures in char [50,56]. As shown in Fig. 4, these two ratios decrease with increasing temperature, indicating that small aromatic ring structures are gradually decomposed into oxygen-containing functional groups or polymerized into larger aromatic rings during gasification. The decrease in $A_{(Gr + VL + Vr)}/A_D$ is slightly more pronounced than in A_{Gr}/A_D, as G_r represents small aromatic rings, while V_L and V_r bands are linked to methylene or methyl groups which are reactive and preferentially consumed at higher temperatures. With increasing RM addition, both ratios initially decrease and then increase, reaching a minimum at an RM addition level of 20 %. At lower RM levels, active sites on RM preferentially adsorb small aromatic ring structures with high reactivity, promoting their decomposition and the formation of oxygen-containing groups. RM also enhances CO_2 production, which participates in cross-linking reactions on the coal and char surfaces. As RM content increases, the yield of CO2 rises, leading to CO_2 adsorption on the coal and char surface and expanding micropores and mesopores [57]. This expansion increases active site vacancies, further promoting the formation of oxygen-containing groups, which are more likely to desorb via C-C bond cleavage and generate smaller aromatic rings and long-chain aliphatic structures. The formation of long-chain aliphatic structures introduces steric hindrance, suppressing small aromatic ring polymerization [58], resulting in an increase in small rings and a corresponding decrease in large ones. Simultaneously, higher RM content also leads to more active sites and the release of lattice oxygen, intensifying the decomposition of large aromatic ring structures, which are rich in free π electrons. These combined effects cause the values of $A_{(Gr + VL + Vr)}/A_D$ and A_{Gr}/A_D to increase gradually.

The ratio of the peak areas of the D band to the G band (A_G/A_D) can reflect the degree of graphitization in char [54]. Generally, higher values correspond to lower graphitization. As shown in Fig. 4, A_G/A_D decreases with temperature, suggesting enhanced graphitization at elevated reaction temperatures. With increasing RM addition, A_G/A_D initially decreases but then increases, aligning with the earlier observation of changes in small aromatic ring structures. While RM accelerates the consumption of active groups like small aromatic rings, it also promotes the decomposition of large aromatic structures with relatively

high reactivity, reducing graphitization. Notably, A_G/A_D stabilizes under both experimental conditions due to the broad D band observed in the Raman spectra of low-rank char. Despite the presence of stable microstructures in the char, such as condensed large aromatic rings, these structures are insufficient to form graphite crystals at low temperatures [54]. The large aromatic ring structures exhibit Raman activity in the D band, and the reduction of defect structures leads to a decrease in the relative Raman intensity of D band. Consequently, A_G/A_D exhibits only slight variations in the later stages as temperature or RM addition increases.

Aromatization of the char structure reduces fluorescence interference and suppresses baseline drift, as shown in Fig. 4(c) and (d). α decreases steadily with temperature, but initially decreases and then increases with RM addition. Coal and char contain substituent groups attached to aromatic ring structures, as well as functional groups containing oxygen, sulfur and nitrogen. These groups are readily consumed during the reaction. Unsaturated olefins and low-condensation aromatic rings, rich in free π-electrons, exhibit a high probability of fluorescence radiation induction [55]. A reduction in α reflects a decrease in polar groups such as oxygen-containing functional groups and weakly condensed aromatic rings. Consequently, α and A_t generally exhibit similar trends. However, at 700 °C, while A_t reaches its minimum, α continues to decline. This behavior likely stems from the significant consumption of aromatic rings rich in free π-electrons at this temperature. Although oxygen-containing functional groups increase, their influence on α is less pronounced than the consumption of aromatic rings. The reduced rate of α decline with increasing RM addition supports this interpretation.

XRD analysis is performed on samples to further investigate changes in the internal carbon structure and crystallinity of the char. Two diffraction peaks are observed in the 20–30° and 40–50° ranges, corresponding to the 002 and 100 planes of carbon, respectively [59]. Deconvolution of the 002 peak allows for the differentiation of amorphous carbon (A-carbon) and turbostratic carbon (T-carbon) in the samples [60]. The 002 peak was fitted using *Peakfit 4.12* software, with a fitting example shown in Fig. 4 (e). The interlayer spacing (d_{002}), lateral size (*La*) and the stacking height of the crystalline (*Lc*) are calculated using the Bragg [61] and Scherrer [62] equations, as defined in Eqs. (12)–(14):

$$Lc = \frac{0.89\lambda}{\beta_{002}\, cos\, \theta_{002}} \tag{12}$$

$$La = \frac{1.84\lambda}{\beta_{100}\, cos\, \theta_{100}} \tag{13}$$

$$d_{002} = \frac{\lambda}{2\, sin\, \theta_{002}} \tag{14}$$

where θ_{002} and θ_{100} present the diffraction angles corresponding to the 002 peak and 100 peak planes, respectively; β_{002} and β_{100} present the full widths at half maximum (FWHM) of the 002 peak and 100 peak, respectively; λ presents the wavelength of the incident X-ray (0.15406 nm)

Fig. 4 (f) and (g) show *Lc*, *La*, and d_{002} for different samples. The results reveal a decrease in d_{002} with increasing temperature, indicating a reduction in interlayer spacing and increased ordering of the carbon layers. As the RM addition ratio increases, d_{002} decreases and then stabilizes, with a more significant reduction in interlayer spacing compared

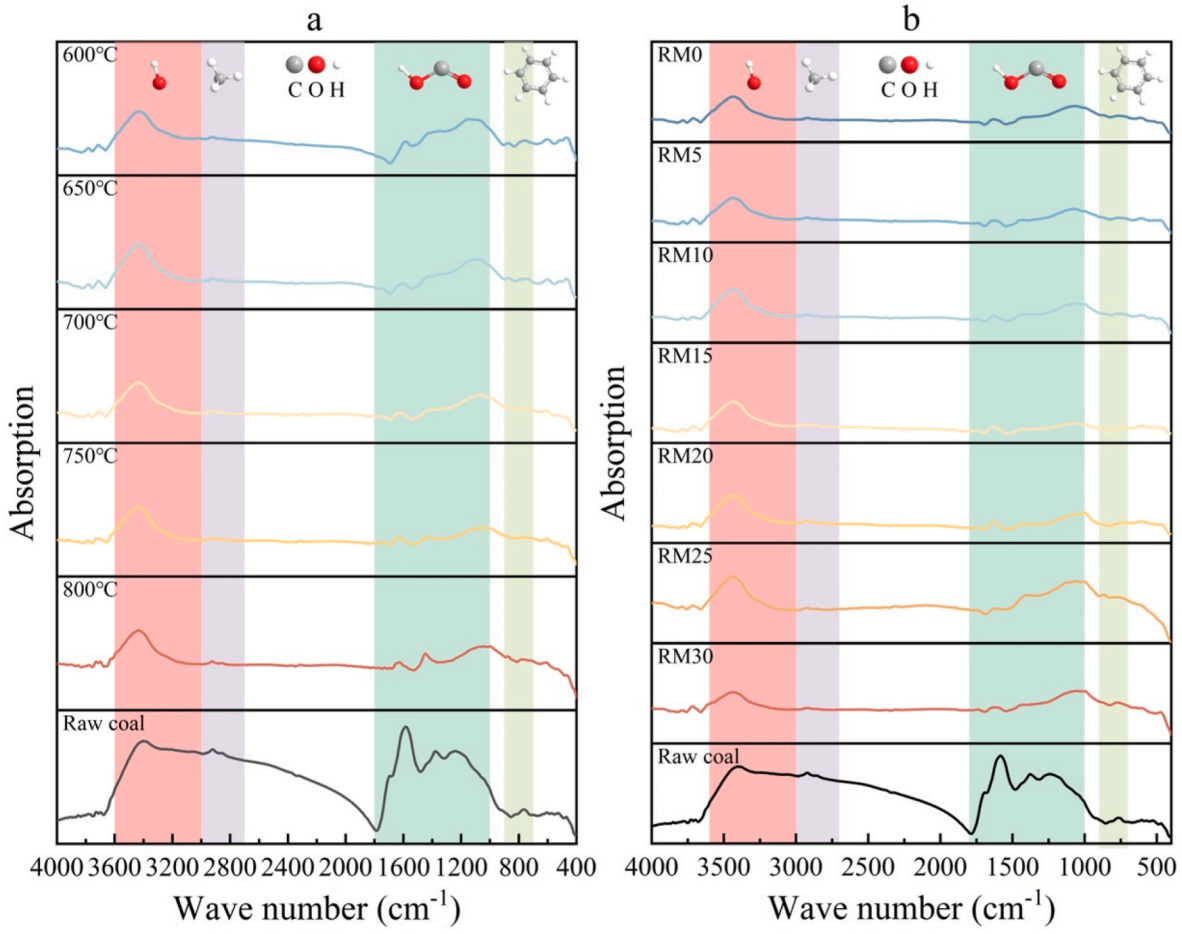

Fig. 5. FTIR spectrum of char samples under different temperatures (a) and RM addition ratios (b).

to temperature increases, suggesting that RM promotes more ordered carbon layer arrangements. Notably, d_{002} remains larger than the theoretical interlayer spacing of graphite (0.34 nm) [63], indicating that the carbon structure in the char is still amorphous and has not fully graphitized. The decrease in *Lc* and increase in *La* with rising temperature reflect the promotion of lateral growth while hindering longitudinal development. High temperatures induce restructuring and cracking reactions that disrupt carbon layers along the c-axis, decreasing *Lc* while promoting condensation of small aromatic rings and the formation of larger aromatic structures, which enhance the lateral growth of carbon layers, thereby increasing *La*. As the RM addition increases, *Lc* decreases consistently, while *La* initially decreases and then increases. This phenomenon is attributed to the promotion of further consumption of small aromatic rings and polar groups by RM, which restricts the longitudinal development of carbon layers and reduces *Lc*. The initial decrease in *La* is linked to the rearrangement and ordering of the carbon structure induced by RM during gasification, coupled with the consumption of high-activity surface structures. However, with higher RM content, additional active sites on RM facilitate the decomposition of large aromatic rings, rich in π-electrons, into smaller aromatic rings. These smaller rings may undergo condensation, leading to lateral expansion of the aromatic structure and an increase in the planar size of the carbon layers. In summary, both temperature and RM addition ratio promote the lateral growth of aromatic layers in the char.

Fig. 4 (h) and (i) present the carbon distribution of samples. T-carbon represents crystalline carbon [64], while A-carbon refers to amorphous carbon in coal that has not yet crystallized. As the temperature and RM addition ratio increase, A-carbon gradually transforms into T-carbon with its percentage decreasing from 53.38 % to 48.89 %. This trend aligns with the changes in d_{002} and A_G/A_D, indicating that A-carbon can reflect the degree of disorder in the char. As discussed in Raman analysis, the transformation of A-carbon into T-carbon is attributed to the conversion of highly active aliphatic groups into aromatic ring structures, which undergo condensation reactions, leading to molecular rearrangements and the formation of T-carbon.

3.2.2. Changes in functional groups of char

To further investigate the effects of reaction conditions on the functional groups and chemical bonds in char, FTIR is performed on the samples as shown in Fig. 5. The FTIR spectra of the samples can be divided into four main regions [65,66]: Hydroxyl (3600-3000 cm^{-1}), Aliphatic hydrocarbons (3000-2700 cm^{-1}), Oxygen-containing functional groups (1800-1000 cm^{-1}), and Aromatic hydrocarbons (900-700 cm^{-1}). Compared to char, raw coal shows significantly stronger peaks in the hydroxyl, aliphatic hydrocarbon, and oxygen-containing functional group regions. In the range of 3600-3000 cm^{-1}, a broad peak around 3440-3433 cm^{-1} is observed in all samples, indicating the presence of pronounced hydroxyl vibrations in each sample, which may result from phenolic, alcohol groups, or water formed during the reaction process [67]. The characteristic peaks in the 1800-1000 cm^{-1} range are attributed to the vibrations of oxygen-containing functional groups such as carbonyls, with variations in peak positions across samples indicating different consumption or interconversion rates of these groups under different conditions. For instance, in reaction **R20**, hydroxyl or carbonyl groups may further react to form relatively thermally stable ether groups, resulting in changes in the characteristic peaks in the 1800-1000 cm^{-1} range. As temperature and RM addition increase, the intensities of peaks in the 3600–3000 cm^{-1} and 1800–1000 cm^{-1} ranges initially decrease and then increase, following the trend observed in the A_t of the samples. This suggests that at low temperatures, oxygen-containing functional groups are consumed preferentially, while at high temperatures, large aromatic structures with

free π-electron configurations undergo pyrolysis, generating new oxygen-containing groups. The addition of RM accelerates the consumption of these functional groups, and at higher RM levels, it catalyzes the decomposition of highly active aromatic structures, resulting in an increased formation of oxygen-containing groups. A similar trend is observed in the 3000-2700 cm^{-1} range. The decomposition of long-chain aliphatic hydrocarbons weakens methyl group vibrations at lower temperatures and RM ratios, as shown in reaction **R21**. At higher temperatures and RM ratios, the decomposition of large aromatic rings and the degradation of oxygen-containing functional groups, such as carboxyl in **R22**, generate small molecular gases and enhance methyl group vibrations, leading to an increase in peak intensity. This dynamic change indicates that the decomposition of aliphatic groups not only generates small molecular gases (e.g., H_2 and C_nH_m) [68] but also triggers new structural evolution. In the 900-700 cm^{-1} range, the number of peaks decreases with increasing temperature and RM addition ratio due to the consumption of small aromatic rings and a reduction in the variety of aromatic structures. However, as indicated in **R23**, the condensation of small aromatic rings into larger structures promotes aromatization and graphitization of the char, which in turn increases the peak intensities.

$$R-COOH+R'-OH \rightarrow R-COO-R'+H_2O \quad \text{R20}$$

$$R-[CH_2]CH_3 \rightarrow R-CH_3+C_nH_m \quad \text{R21}$$

$$R-C(CH_3)_2-COOH \rightarrow R-CH(CH_3)_2+CO_2 \quad \text{R22}$$

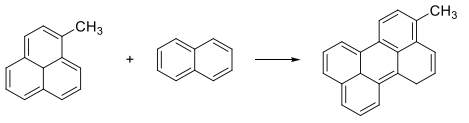

R23

XPS analysis of the C 1s and O 1s spectra is performed to investigate the transformation patterns of oxygen-containing functional groups in the coal during the reaction [69]. Energy calibration is conducted using the C 1s peak at 284.8 eV, and the C 1s and O 1s spectra are deconvoluted using *Avantage* software. Based on the specific assignments of these characteristic peaks summarized in Table S3, the C 1s spectrum and O 1s spectra can be respectively divided into five and three characteristic peaks. The fitting examples are shown in Fig. 6(a) and (b). Fig. 6(c)–(f) show the distribution of C-containing and O-containing functional groups in the different samples.

The five characteristic peaks observed in the C 1s spectrum corresponding to graphitized carbon (C=C, 284.69 ± 0.3 eV), aliphatic carbon (C-C and C-H, 285.32 ± 0.3 eV), carbon-oxygen single bonds in phenolic, alcoholic, and ether groups (C-O, 286.11 ± 0.3), carbon-oxygen double bonds in carbonyl groups (C=O, 287.54 ± 0.3 eV), and

carboxyl groups (O-C=O, 289.04 ± 0.3 eV). The primary carbon forms in the char were graphitized and aliphatic carbon, accounting for over 72 % of the total carbon content. As the temperature increased, graphitized carbon increased and aliphatic carbon decreased due to the poor thermal stability of aliphatic hydrocarbons, with similar trends observed for RM addition. The C-O content first decreases and then increases, reaching a maximum of 14.95 %. This is primarily due to the oxidation of alcohol groups to carboxyl groups (O-C=O) at high temperatures and the conversion of some hydroxyl groups to thermally stable ether groups(C-O-C), increasing C-O bonds. The changes in the relative content of C-O bonds with increasing RM addition can be attributed to similar reasons. The relative content of C=O groups increased with temperature and RM addition, then decreased, likely due to the differing decomposition rates of carbonyl groups and the formation rates of thermally stable ketones. As noted previously, excessive RM significantly catalyzes the decomposition of these groups, reducing their relative content. In summary, the changes in the relative content of these functional groups in the C 1s spectra are consistent with the FTIR results.

In the O 1s spectrum, the C=O group (carbonyl, carboxyl, lactone) appeared at 531.8 ± 0.5 eV, the epoxy group (C-O) at 532.6 ± 0.5 eV, and the ether (C-O-C) and hydroxyl (-OH) groups at 533.7 ± 0.5 eV [70].

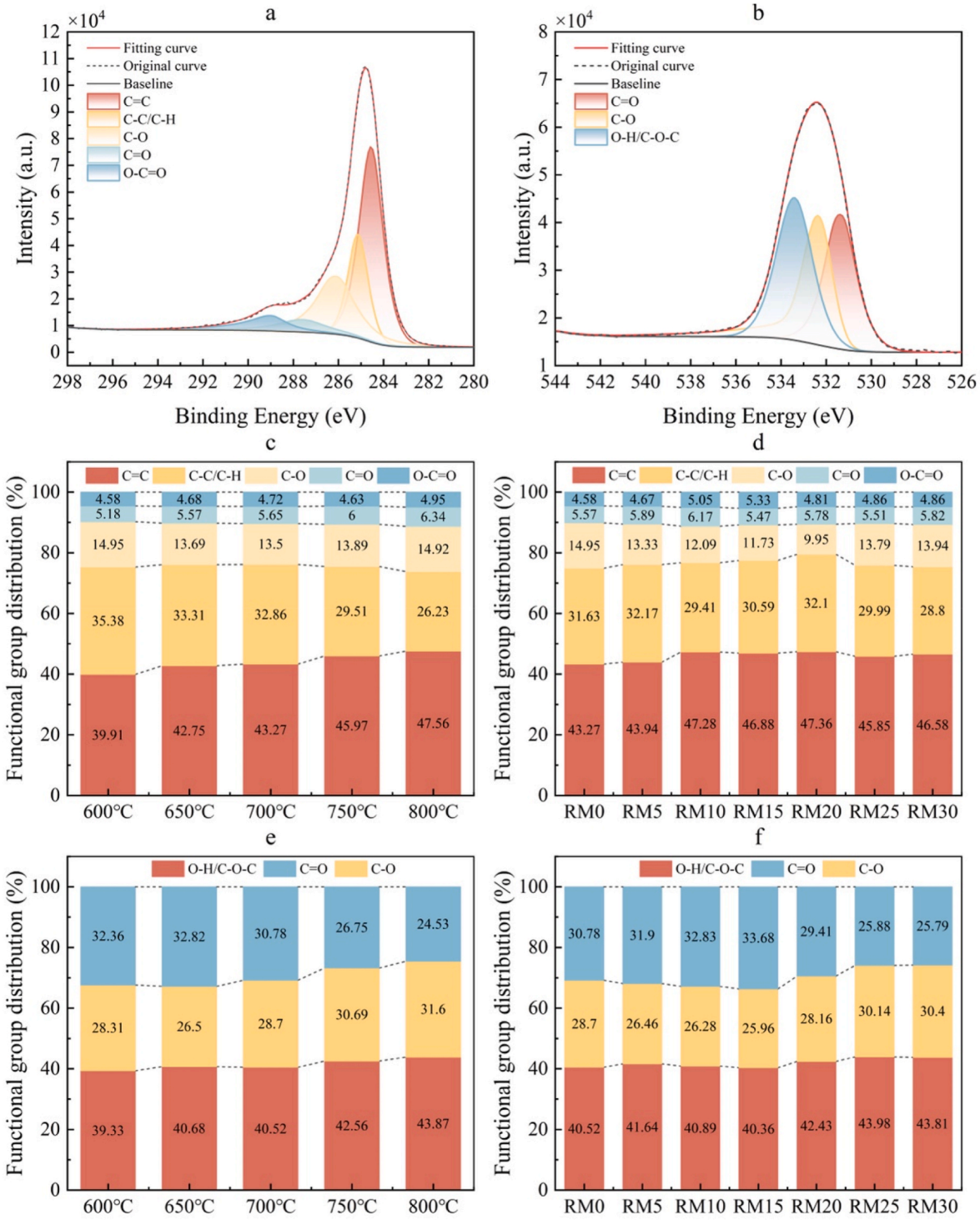

Fig. 6. XPS fitting examples and results of the samples: a–c: C 1s spectra; d–f: O 1s spectra.

The relative content of the epoxy group first decreases and then increases with changes in both experimental conditions, mirroring the same reasons and trend observed in the C 1s spectrum analysis. The relative content of hydroxyl and ether groups remains constant initially, then increases with temperature. It is hypothesized that during the low-temperature stage, ether groups with better thermal stability are formed from the conversion of partial hydroxyl groups, which leads to the relative content of -OH and C-O-C remaining constant. At higher temperatures, the dynamic equilibrium shifts toward the generation of hydroxyl due to the oxidation of aromatic structures and aliphatic carbon chains, leading to an increase in the relative content of -OH and C-O-C bonds. The content of carbonyl, carboxyl, and lactone groups decreases after an initial stable phase with increasing temperature and RM addition, possibly due to the decomposition of lactone groups attached to aliphatic hydrocarbons and aromatic ring structures at high temperatures or with higher RM addition.

3.2.3. *Pore characteristics and reactivity of char*

The pore characteristic parameters of the char samples are presented in Table 6. The result shows that, under a constant equivalence ratio, the

Table 6
Specific surface area and pore characteristic parameters of char samples.

Cases	$S_{bet}(m^2/g)$	$S_{mic}(m^2/g)$	$V_{total}(cm^3/g)$	$V_{mic}(cm^3/g)$
1	225.187	196.937	0.1055	0.0734
2	241.027	205.951	0.1143	0.0818
3	245.087	214.782	0.1119	0.0853
4	247.759	218.066	0.1181	0.0873
5	213.778	187.057	0.1014	0.0684
6	254.549	221.485	0.1182	0.0880
7	265.557	226.555	0.1227	0.0900
8	302.251	260.031	0.1398	0.1034
9	308.397	267.669	0.1380	0.1062
10	236.490	205.130	0.1080	0.0815
11	230.646	197.901	0.1070	0.0786

Note: S_{bet} is the BET specific surface area; S_{mic} is the micropore specific surface area; V_{total} is the total pore volume; V_{mic} is the micropore volume.

pore characteristic parameters first increase and then decrease with rising temperature, peaking at 750 °C. This can be attributed to the enhanced release of volatiles and oxidation reactions at lower temperatures, which promote micropore formation and increase the specific surface area. At higher temperatures, intensified polycondensation reactions within the char lead to pore collapse and structural densification, resulting in a reduced surface area. Notably, a significant increase in BET surface area is observed between 600 °C and 650 °C. Combined with CO_2 yield analysis, this may be due to CO_2 participating in cross-linking reactions on the char surface [57], further expanding the pore network. At 800 °C, a sharp decline in specific surface area occurs, likely due to the combined effects of CO_2 conversion to CO and intensified char polycondensation at elevated temperatures. With increasing RM addition, the pore characteristic parameters of char also exhibit a rise-then-fall pattern. Moderate RM promotes gasification and pyrolysis of coal char, enhancing micropore development and surface area. Excessive RM leads to over-catalysis, causing structural breakdown and pore collapse or blockage, thereby reducing surface area. Notably, the variation of pore parameters deviates from the CO_2 yield trend at this temperature, indicating that excessive RM catalytic activity plays a dominant role in pore structure evolution.

According to our previous studies [48,71], the reactivity of char can be assessed using thermogravimetric analysis (TGA). The char reactivity coefficient(R) is calculated, with a higher R value indicating stronger combustion reactivity. As shown in Fig. 7, cbar reactivity decreases with increasing reaction temperature. This trend is attributed to the acceleration of volatile matter release and fixed carbon reactions at elevated temperatures, which promote the structural ordering of char and consequently reduce its reactivity. With increasing RM addition, the char reactivity exhibits a non-monotonic "N-type" trend, similar to the pattern observed in Raman structural parameters. Conversely, this behavior is inconsistent with the variation in BET surface area under the same conditions, which indicates that the reactivity of char may not have a strong correlation with the specific surface area of BET.

To further investigate the relationship between coke reactivity and its physicochemical structure, Pearson correlation coefficients (r) were calculated using SPSS software according to Eq. (15). The correlation coefficient ranges from −1 to +1, indicating negative or positive correlation, respectively. A significance threshold of $P < 0.05$ was adopted to assess statistical relevance [72].

$$r = \frac{\sum (X-\overline{X})(Y-\overline{Y})}{\sqrt{\sum (X-\overline{X})^2}\cdot\sqrt{\sum (Y-\overline{Y})^2}} \tag{15}$$

where X and Y represent the values of the two variables; $\overline{X}$ and $\overline{Y}$ represent their respective mean values.

The calculation results are shown in Table 7. The results show that char reactivity exhibits a strong positive correlation with both $I_{(Gr+VL+Vr)}/I_D$ and α, with a statistically significant value of P below 0.05. In contrast, other structural parameters, including BET surface area and crystallographic features, show weaker correlations with reactivity. These findings suggest that the combustion reactivity of char is primarily governed by its chemical structure, particularly by highly reactive small aromatic ring structures and oxygen-containing functional groups. The more condensed the chemical structure becomes, the lower the char reactivity. Additionally, the development of pore structure and crystallinity shows a limited or even negative correlation with reactivity. This discrepancy can be explained by the fact that BET surface area reflects only the physical porosity, but does not account for all reactive sites, which can dominate the reactivity of char [73]. These reactive sites are

Table 7
Pearson correlation analysis results.

Parameters	r	P
S_{bet}	−0.3858	0.2413
S_{mic}	−0.4077	0.2133
$I_{(Gr+VL+Vr)}/I_D$	0.8771	0.0004
I_{total}	0.0220	0.9488
α	0.7732	0.0053
d_{002}	0.2924	0.3829
Lc	0.4350	0.1811
La	−0.5717	0.0661

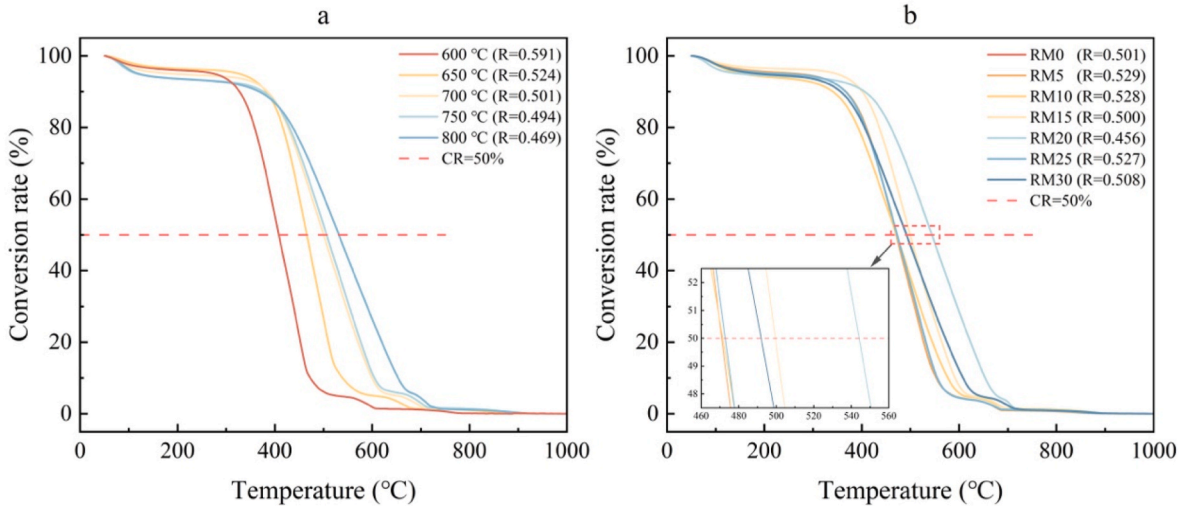

Fig. 7. TG curves and reactivity coefficients of char samples under different temperatures (a) and RM addition ratios (b).

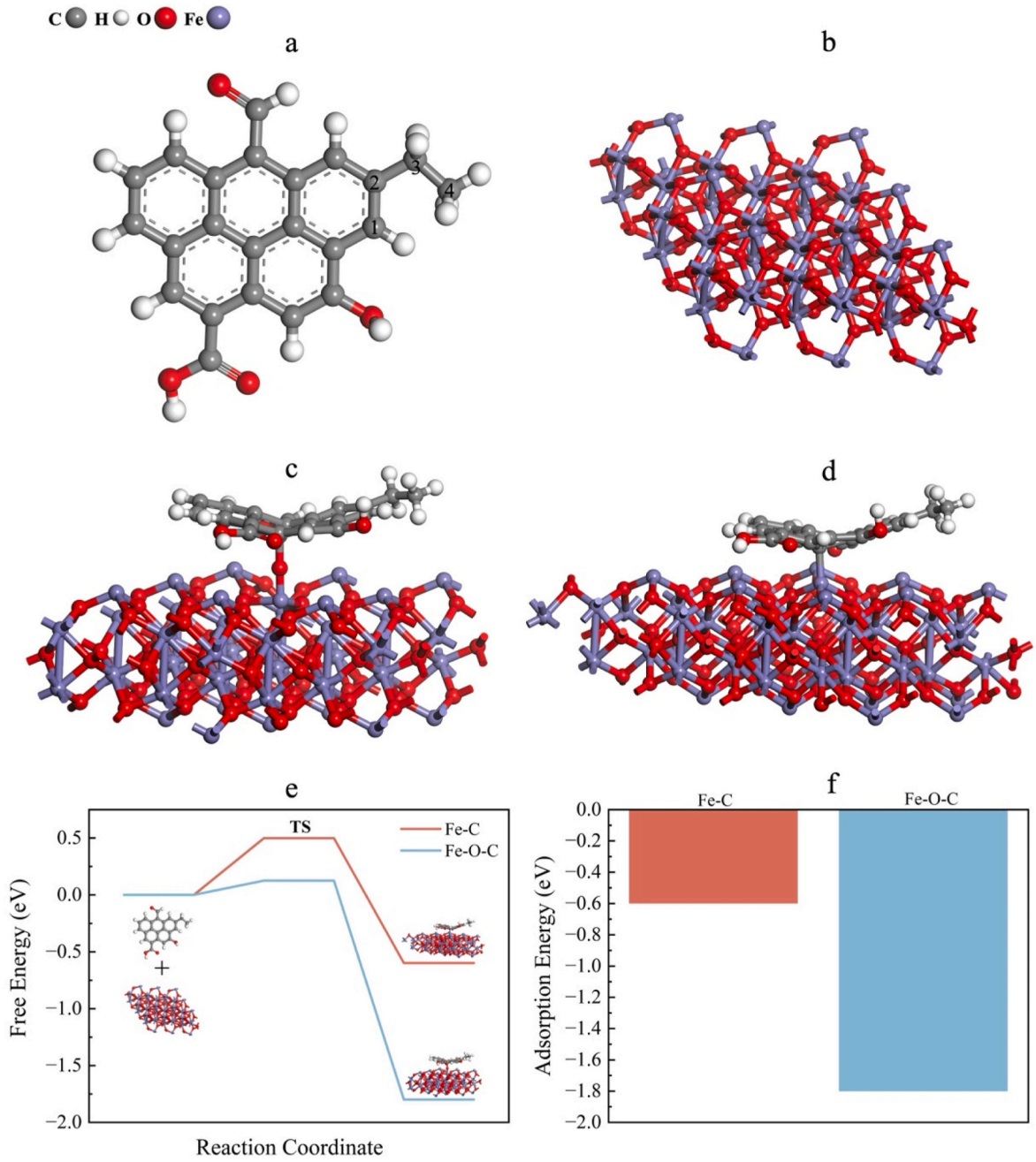

Fig. 8. a: Schematic of MSC structure; b: α-Fe_2O_3; c: MSC@Fe-O-C; d: MSC@Fe-C; e: Free energy diagram for two adsorption configurations; f: Adsorption energies of the two configurations.

likely concentrated at edge defects, amorphous carbon zones, or heteroatom-doped regions, which are not fully captured by surface area measurements alone. Similarly, although the crystallographic parameters provide an indication of carbon structure ordering, the presence of local defects or potential reactive sites may cause deviations between char reactivity and crystallographic parameter trends [74].

3.3. DFT calculation of RM catalytic gasification

3.3.1. Model building and simulation of adsorption morphology

This study employs Density Functional Theory (DFT) to investigate the catalytic pathways of RM-catalyzed gasification. As shown in Table S4, studies by many scholars have demonstrated that Fe_2O_3 is identified as the primary catalytic component in RM for lignite partial gasification. And the catalytic activity of Fe_2O_3 surpasses that of other main components such as Al_2O_3 and SiO_2, which exhibit limited or indirect effects on gasification under the studied conditions. Consequently, hematite (α-Fe_2O_3), the primary form of Fe_2O_3 in RM, is selected for DFT calculation. While the structure of actual coal char is highly complex, DFT calculations encounter huge difficulties in accurately simulating large multi-atomic systems while ensuring computational feasibility [75]. Lignite-derived aromatics primarily contain 1-3 condensed rings [76], and during coal-to-char conversion, single benzene ring clusters tend to grow into small polycyclic aromatic hydrocarbons (PAHs) [77]. Meanwhile, previous studies on gasification [78, 79] have demonstrated that PAH models with 4–7 benzene rings can effectively represent coal char, with the number of graphite rings having no bearing. Thus, as shown in Fig. 8 (a) and (b), a model with five benzene rings (denoted MSC) is chosen, and oxygen-containing functional groups and aliphatic hydrocarbons are added to simulate the

typical functional group distribution characteristics in coal char.

This study primarily investigates the adsorption process between the hematite and MSC model, as well as the reaction with oxygen after adsorption. Research by Nelson Y. Dzade et al. [80] suggests that the parallel adsorption geometry of benzene molecules on the hematite surface is more stable than vertical adsorption, primarily due to π-bond interactions between the benzene and hematite. The exposed Fe or O atoms on the α-Fe_2O_3 surface can serve as active adsorption sites for the benzene rings in the MSC model. Two types of coordination adsorption, Fe-C and Fe-O-C, are analyzed. The two structures are denoted as MSC@Fe-O-C and MSC@Fe-C, as shown in Fig. 8(c) and (d). The calculations show that the C-C bond length in the MSC model is 1.540 Å, while adsorption induces bending and deformation which causes the C-C bond length of the MSC to vary from 1.469 Å to 1.842 Å. In the MSC@Fe-C structure, the Fe-C bond length is 1.909 Å, while in the MSC@Fe-O-C structure, the Fe-O and O-C bond lengths are 1.602 Å and 1.598 Å, respectively. These results indicate that the O atom, acting as a bridge, shortens the coordination bond lengths between α-Fe_2O_3 and MSC. Shorter bond lengths generally correspond to higher bond energies, which enhance the stability of the adsorption structure.

Fig. 8 (e) and (f) show the energy barrier and adsorption energy data for both adsorption modes. The energy barrier for transition state (TS) formation via Fe-O-C coordination is lower, with the final energy barrier for the MSC@Fe-O-C structure is also lower than that for the MSC@Fe-C structure. This suggests that the Fe-O-C coordination bond adsorption mode is more favorable than the Fe-C coordination bond mode. The adsorption energies of MSC@Fe-C and MSC@Fe-O-C are −0.59 eV and −1.79 eV, respectively, which indicate that both are exothermic processes. The difference in adsorption energy can be attributed to the physicochemical properties of α-Fe_2O_3. As a typical transition metal oxide, the coordination-unsaturated Fe atoms on its surface exhibit strong Lewis acidity [81], capable of accepting electron pairs. The free π-electron cloud on the benzene ring is a good electron donor. In the Fe-C coordination, the interaction between Fe and the π-electron cloud lowers the free energy of the system and releases heat, resulting in a negative adsorption energy. For Fe-O-C coordination, the O atom on α-Fe_2O_3 enhances the Fe-C interaction with its lone pair electrons, forming a covalent bond with the C atom in the benzene ring. This multi-interaction makes Fe-O-C stronger, increasing adsorption energy. Additionally, the O atom serves as a "bridge," shortening the coordination bond, increasing bond energy, and providing a more flexible geometric arrangement, which helps reduce local stress during the coordination process. Therefore, for subsequent calculations, MSC@Fe-O-C with MSC was selected for DFT analysis in the partial gasification process with O_2.

3.3.2. Analysis of RM catalytic pathway

To reveal the reaction mechanisms of coal char during SC gasification, this study systematically simulated O_2 adsorption and subsequent micro-reaction pathways on both pristine MSC and Fe_2O_3-modified MSC@Fe-O-C systems. The computed reaction pathways and energy barrier diagrams are illustrated in Fig. 9. Both systems exhibit three-stage reaction sequences: (1) adsorption of O_2, (2) cleavage of the C-C bond in the benzene ring, and (3) O_2 diffusion. In Stage 1, O_2 molecules adsorbed on carbon atoms in MSC and iron atoms in MSC@Fe-O-C, with adsorption energies of −0.32 eV and −0.54 eV, respectively. This

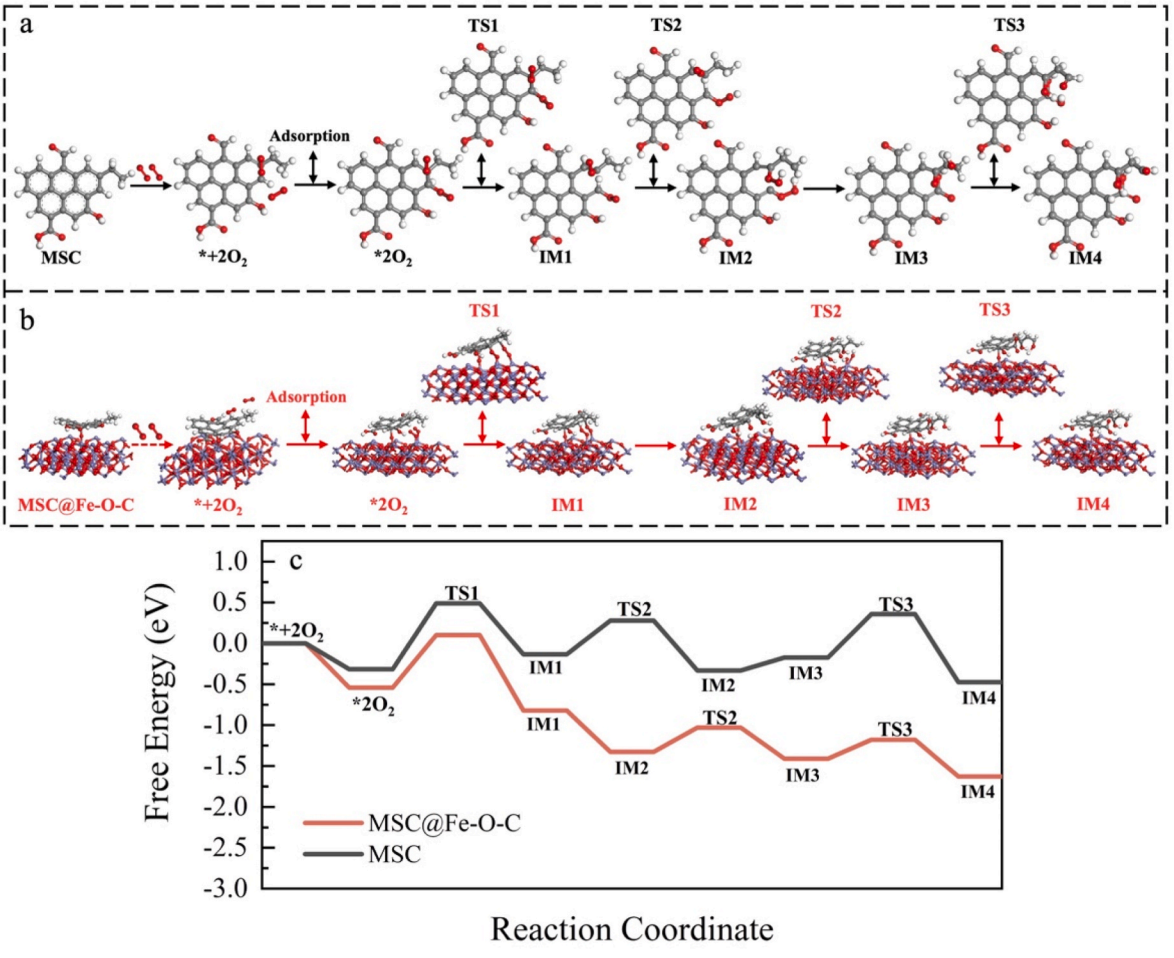

Fig. 9. a: Reaction pathway of the MSC system; b: Reaction pathway of the MSC@Fe-O-C system; c: Free energy profiles of the reactions in both systems.

indicates that Fe_2O_3 can enhance O_2 adsorption on coal char.

As shown in Fig. 9 (a), for the MSC system, post-adsorption thermal effects induce benzene ring distortion into the transition state TS1. During this process, C-C bonds in the benzene ring where C1 and C2 atoms are located exhibit length variations ranging from 1.454 Å to 1.996 Å. Subsequent C1-C2 bond cleavage generates radicals on both carbon atoms (denoted as IM1). Unbound O atoms in O_2, which are not connected to the carbon atoms, electrostatically attracted hydrogen atoms from methyl groups and the original benzene ring, forming hydroxyl groups. O-O bond dissociation then produces two free hydroxyl groups that adsorb on C1 and C4 atoms, forming the IM2. Concurrently, a carboxyl group formed at C2. Attraction between O and H atoms caused the H atom on C4 to become a radical, bonding with residual O on C1 to form another hydroxyl group, while C4 transforms into an aldehyde group (IM4). This evolution demonstrates that O_2 participation disrupts aromatic clusters in the coal char while increasing oxygen-containing functionalities like hydroxyl groups.

As shown in Fig. 9 (b), for the MSC@Fe-O-C system, the adsorption of O_2 is facilitated by the Fe2O3 bridge, which induces changes in the C-C bond lengths of the MSC structure. The bond length stretches to a maximum of 1.996 Å and contracts to a minimum of 1.454 Å. Therefore, it is hypothesized that the energy required to break the C-C bonds in MSC@Fe-O-C is lower compared to MSC alone. The Fe-adsorbed O_2 forms covalent bonds with adjacent C atoms (IM1). Subsequent O-O bond cleavage at the Fe site generates hydroxyl groups through hydrogen abstraction from C4. Simultaneous thermal cleavage of C1-C2 bonds facilitates O-H formation at C2 (IM2).In the next step, the Fe-bound hydroxyl groups migrate to the C4 and C2 atoms(IM3). Ultimately, as in the MSC pathway, a carboxyl group forms on C2, while C4 transforms into an aldehyde group, forming the IM4 structure. The free energy diagram reveals lower energy states throughout the MSC@Fe-O-C reaction compared to MSC are illustrated in Fig. 9(c). The respective highest-energy barriers of 0.82 eV (MSC@Fe-O-C) and 0.93 eV (MSC) confirm that Fe_2O_3 reduces reaction barriers, facilitating the gasification reaction between O_2 and the coal char, which is consistent with experimental observations.

3.4. Reaction mechanism analysis

The combined characterization and DFT calculations reveal the mechanistic effects of temperature and RM on the partial gasification of SC with O_2 (Fig. 10). Under a fixed equivalence ratio, with the increase in temperature, gasification reactions such as the Boudouard reaction are intensified which accelerates the cracking of macromolecular structures in SC into smaller fragments, thereby increasing the production of combustible gas components (CGC). At low-temperature stages, the highly reactive oxygen-containing functional groups and small aromatic clusters in SC are preferentially consumed, with their consumption rate exceeding the generation rate, leading to a decrease in oxygenated group content in the char. However, as the temperature rises to the high-temperature stage, the thermal decomposition of large aromatic ring structures generates new small aromatic clusters. Simultaneously, the enhanced reaction rate of gasification at elevated temperatures promotes oxidative reactions with aromatic structures, producing additional oxygen-containing functional groups. In this regime, the formation rate of oxygenated groups surpasses their consumption rate, resulting in an increase in their content within the char. This process is accompanied by the structural disordering of char.

Regarding the catalytic mechanism of RM, the main active component in RM, hematite (α-Fe_2O_3), adsorbs onto the MSC structure through spontaneous Fe-O-C coordination. DFT calculations demonstrate that α-Fe_2O_3 reduces the energy barrier for partial gasification by 11.83 % compared to non-catalytic conditions, confirming its role in catalyzing the partial gasification of SC. As a result, with the addition of RM, the gasification of SC is enhanced, the decomposition of macromolecular structures in SC is promoted, and more small molecules are released, ultimately increasing the CGC yield. Due to the same reason, under the catalytic effect of RM, the large molecular structures in SC undergo catalytic decomposition, generating more oxygen-containing functional groups. With the increase in RM, more active sites are provided, and these oxygen functional groups are consumed during the reaction. However, as the proportion of RM increases further, more active sites and lattice oxygen are provided, leading to the decomposition of large aromatic ring structures (MAC) in SC into small aromatic ring structures, accompanied by the generation of oxygenated functional groups. Ultimately, oxygenated group concentration exhibits a characteristic N-

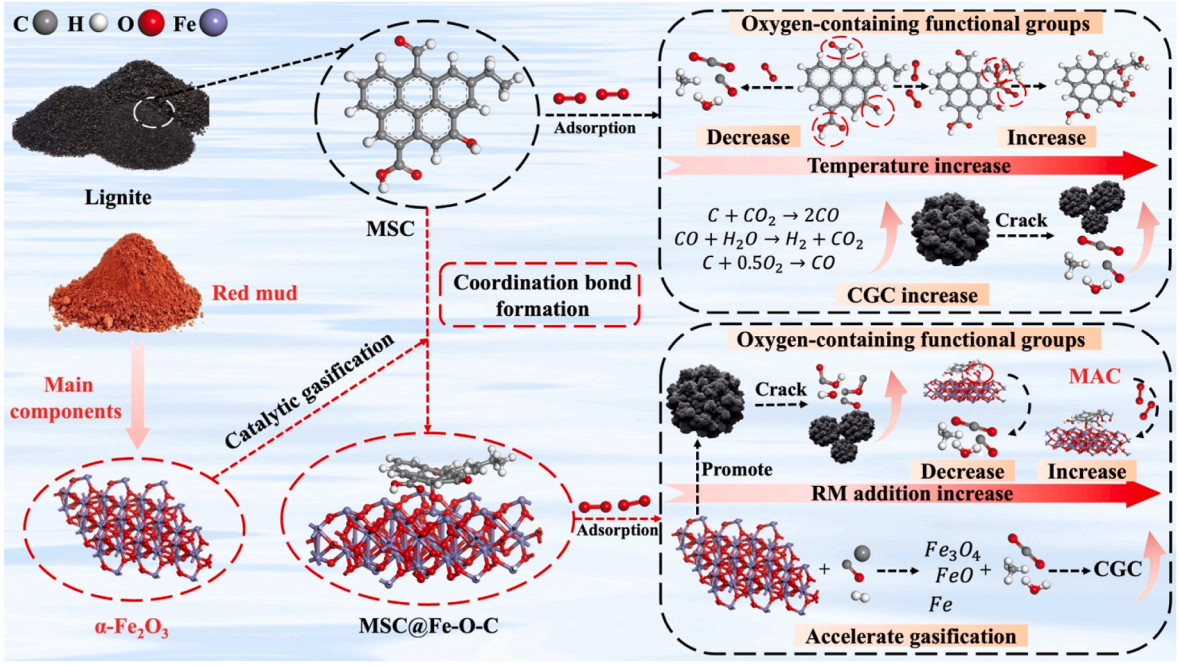

Fig. 10. Reaction mechanism diagrams of SC partial gasification and RM catalytic partial gasification.

shaped trend versus RM addition ratio.

3.5. Limitations of this study

This work combined experiments and DFT calculations to reveal the effects and mechanisms of RM addition and temperature on lignite partial gasification, offering insights into char structure evolution and catalytic pathways. However, several limitations should be acknowledged. As follows.

(1) Although RM has demonstrated its potential to lower the reaction temperature, its contribution to CO_2 emission reduction has only been demonstrated indirectly, without a theoretical calculation model for direct quantification in this work;
(2) The data samples are limited due to time constraints may affect the reliability of the correlations between char reactivity and other parameters;
(3) Owing to limitations in computational power, the DFT calculations were restricted to the PAH model, which may not fully represent the complexity of real coal char structures.

To address the aforementioned limitations and further refine this research, future studies should incorporate larger datasets, structurally representative models, and comprehensive life cycle assessments of CO_2 emissions.

4. Conclusions

In this study, partial gasification experiments of SC were conducted under varying temperatures and RM addition ratios. Combined with quantum chemical calculations, the effects of the temperature and RM addition ratio on the properties of char and syngas and the underlying mechanisms were investigated. The main conclusions are as follows.

(1) Increasing temperature and RM addition significantly enhanced the syngas yield and reduced the char yield, with the syngas yield rising by 13.99 % and 5.07 %, respectively. Elevated temperatures promoted CO and H_2 formation, whereas RM additives primarily facilitated H_2 generation. Consequently, the CGC yields increased by 416.49 mL/g and 47.93 mL/g under varying temperatures and RM addition ratios. Compared with the increased CO_2 emissions caused by raising the ER to elevate reaction temperature in industrial applications, the addition of RM lowers the reaction temperature while maintaining syngas quality, thereby indirectly reducing CO_2 emissions.
(2) Both temperature and RM addition influenced the structural evolution of char. Elevated temperatures enhanced the graphitization and lateral growth of char. As the temperature rose, oxygen-containing groups in the char first decreased and then increased. Initially, elevated temperatures decomposed small aromatic clusters and oxygen-containing groups. At higher temperatures, large aromatic systems broke down, regenerating these oxygen-containing groups. The addition of RM contributed to the lateral growth of char by providing active sites and releasing lattice oxygen, thereby promoting the breakdown of carbon structures. At low RM levels, oxygen-containing groups increased, but more RM led to their consumption and later regeneration because of the increase in active sites until excessive. These mechanisms together resulted in an N-shaped trend in the oxygen-containing group content in char as a function of RM addition.
(3) The BET surface area and pore parameters of char showed non-monotonic variations with temperature, initially increasing through volatile release and the oxidation reactions, then decreasing for polycondensation reactions of carbon structures. Pore characteristics also followed a rise-then-fall trend with increasing RM addition. Moderate RM similarly induced peak pore development, while excess RM caused structural failure. Although char reactivity declined with temperature because of the graphitization of carbon structure, it exhibited an N-shaped trend with increasing RM. This discrepancy indicated that the reactivity of char was primarily influenced by its chemical structure, while BET surface area and crystal structure did not fully reflect the number of reactive sites in char, thus showing weak correlation with combustion reactivity.
(4) DFT calculation revealed the catalytic mechanisms of the key component in RM, α-Fe_2O_3. α-Fe_2O_3 forms Fe-O-C coordination bonds with SC, causing deformation of the benzene ring structures in the char and lowering their bond dissociation energy. α-Fe_2O_3 acts as a bridge to adsorb O_2, reducing the adsorption energy of O_2 from −0.32 eV to −0.54 eV. This catalytic bridge effect lowered the activation barrier for gasification reactions through efficient O_2 transfer from α-Fe_2O_3 to coal char.

CRediT authorship contribution statement

Bin Zhang: Writing – review & editing, Writing – original draft, Visualization, Methodology, Investigation, Conceptualization. **Zhihua Tian:** Writing – review & editing, Investigation. **Qinhui Wang:** Supervision, Resources, Funding acquisition, Conceptualization. **Ruiqing Jia:** Supervision, Investigation. **Dong Ma:** Supervision, Investigation. **Xie Guilin:** Supervision.

Declaration of competing interest

The authors declare that they have no known competing financial interests or personal relationships that could have appeared to influence the work reported in this paper.

Acknowledgement

Thanks for the financial supported by the Fundamental Research Funds for the Central Universities, China (2022ZFJH004).

Appendix A. Supplementary data

Supplementary data to this article can be found online at https://doi.org/10.1016/j.energy.2025.136352.

Data availability

Data will be made available on request.

References

[1] Statistical Review of World Energy 2024. Energy Inst 2024;3.
[2] Zhao P, Zhong L, Zhu R, Zhao Y, Luo Z, Yang X. Drying characteristics and kinetics of Shengli lignite using different drying methods. Energy Convers Manag 2016; 120:330–7. https://doi.org/10.1016/j.enconman.2016.04.105.
[3] Liu P, Zhang D, Wang L, Zhou Y, Pan T, Lu X. The structure and pyrolysis product distribution of lignite from different sedimentary environment. Appl Energy 2016; 163:254–62. https://doi.org/10.1016/j.apenergy.2015.10.166.
[4] Li C-Z. Some recent advances in the understanding of the pyrolysis and gasification behaviour of Victorian brown coal. Fuel 2007;86:1664–83. https://doi.org/10.1016/j.fuel.2007.01.008.
[5] Li X, Wang D, Yu J, Wang J, Wang B, Li P, et al. Catalytic effects of red mud on coal char gasification and the transformation of active lattice oxygen in iron oxides. Fuel 2025;380:133241. https://doi.org/10.1016/j.fuel.2024.133241.
[6] Zhang G, Yang Y, Jin H, Xu G, Zhang K. Proposed combined-cycle power system based on oxygen-blown coal partial gasification. Appl Energy 2013;102:735–45. https://doi.org/10.1016/j.apenergy.2012.08.019.
[7] Zhou Jing, Zhong Huang, Xiao R. Air and steam coal partial gasification in an atmospheric fluidized bed. Energy Fuels 2005;19:1619–23. https://doi.org/10.1021/ef0497558.
[8] Song X, Wang Q, Zhu Y, Xie G, Zhu D, Cen J, et al. Experimental study on coal partial gasification coproducing char, tar, and gas. J Therm Sci 2023;32:2297–309. https://doi.org/10.1007/s11630-023-1832-9.

[9] Chen Z, Dun Q, Shi Y, Lai D, Zhou Y, Gao S, et al. High quality syngas production from catalytic coal gasification using disposable Ca(OH)2 catalyst. Chem Eng J 2017;316:842–9. https://doi.org/10.1016/j.cej.2017.02.025.

[10] Bai Y, Lv P, Li F, Song X, Su W, Yu G. Investigation into Ca/Na compounds catalyzed coal pyrolysis and char gasification with steam. Energy Convers Manag 2019;184:172–9. https://doi.org/10.1016/j.enconman.2019.01.063.

[11] Zhao D, Liu H, Lu P, Sun B, Guo S, Qin M. DFT study of the catalytic effect of Fe on the gasification of char. Fuel 2021;292:120203. https://doi.org/10.1016/j.fuel.2021.120203.

[12] Zhou X, Zhang L, Chen Q, Xiao X, Wang T, Cheng S, et al. Study on the mechanism and reaction characteristics of red-mud-catalyzed pyrolysis of corn stover. Fuel 2023;338:127290. https://doi.org/10.1016/j.fuel.2022.127290.

[13] Wang M, Wei G, Yang S, Zhu R, Yang L. Effect of alkali (K/Na) metal vapor on the metallurgical properties of coke in CO2–O2–N2 mixed atmosphere. Energy 2022;257:124748. https://doi.org/10.1016/j.energy.2022.124748.

[14] Feng J, Xue X, Li X, Li W, Guo X, Liu K. Products analysis of Shendong long-flame coal hydropyrolysis with iron-based catalysts. Fuel Process Technol 2015;130:96–100. https://doi.org/10.1016/j.fuproc.2014.09.035.

[15] Min Z, Asadullah M, Yimsiri P, Zhang S, Wu H, Li C-Z. Catalytic reforming of tar during gasification. Part I. Steam reforming of biomass tar using ilmenite as a catalyst. Fuel 2011;90:1847–54. https://doi.org/10.1016/j.fuel.2010.12.039.

[16] Fu Y, Guo Y, Zhang K. Effect of three different catalysts (KCl, CaO, and Fe2O3) on the reactivity and mechanism of low-rank coal pyrolysis. Energy Fuels 2016;30:2428–33. https://doi.org/10.1021/acs.energyfuels.5b02720.

[17] Shi P, Chang G, Tan X, Guo Q. Enhancement of bituminous coal pyrolysis for BTX production by Fe2O3/MoSi2-HZSM-5 catalysts. J Anal Appl Pyrolysis 2020;150:104867. https://doi.org/10.1016/j.jaap.2020.104867.

[18] Lahijani P, Zainal ZA, Mohamed AR, Mohammadi M. CO2 gasification reactivity of biomass char: catalytic influence of alkali, alkaline earth and transition metal salts. Bioresour Technol 2013;144:288–95. https://doi.org/10.1016/j.biortech.2013.06.059.

[19] Jiang L, Hu S, Wang Y, Su S, Sun L, Xu B, et al. Catalytic effects of inherent alkali and alkaline earth metallic species on steam gasification of biomass. Int J Hydrogen Energy 2015;40:15460–9. https://doi.org/10.1016/j.ijhydene.2015.08.111.

[20] Geng P, Zhang Y. Calcium deactivation during the char-CO2 gasification and its influence on determining the apparent reaction orderchar-CO2. Chem Eng J 2020;395:124955. https://doi.org/10.1016/j.cej.2020.124955.

[21] Wang G, Wang Y, Lv J, Wu Y, Jin L, Li Y, et al. Effect of red mud-based additives on the formation characteristics of tar and gas produced during coal pyrolysis. J Energy Inst 2022;104:1–11. https://doi.org/10.1016/j.joei.2022.06.009.

[22] Khairul MA, Zanganeh J, Moghtaderi B. The composition, recycling and utilisation of Bayer red mud. Resour Conserv Recycl 2019;141:483–98. https://doi.org/10.1016/j.resconrec.2018.11.006.

[23] Li F, Yu B, Fan H, Guo M, Wang T, Huang J, et al. Investigation on regulation mechanism of red mud on the ash fusion characteristics of high ash-fusion-temperature coal. Fuel 2019;257:116036. https://doi.org/10.1016/j.fuel.2019.116036.

[24] Sushil S, Batra VS. Catalytic applications of red mud, an aluminium industry waste: a review. Appl Catal B Environ 2008;81:64–77. https://doi.org/10.1016/j.apcatb.2007.12.002.

[25] Zhou X, Cheng S, Li Y, Yang C, Zhang L, Xiao X, et al. Characterization and mechanism of red-mud-catalyzed steam gasification of corn stover. Fuel 2024;356:129611. https://doi.org/10.1016/j.fuel.2023.129611.

[26] Li X, Chang G, Yang L, Wang C. Enhancement of coke gasification by lignite and a low-cost Fe/red mud catalyst to produce syngas. J Energy Inst 2021;98:116–23. https://doi.org/10.1016/j.joei.2021.06.004.

[27] Lee S, Eun Lee J, Jong Lee S, Wook Lee J, Yun Y, Park N-K, et al. Synergistic desulfurization performance of industrial waste Red mud: a comprehensive experimental and computational study for COS removal and CO(g) production. Appl Surf Sci 2024;649:159132. https://doi.org/10.1016/j.apsusc.2023.159132.

[28] Huang Y-M, Cheng Y-C. Adsorption and C–C bond cleavage of benzene on hematite α-Fe2O3 surfaces: a DFT mechanistic study. Sci Rep 2024;14:22488. https://doi.org/10.1038/s41598-024-73307-w.

[29] Investigation on the impact of air equivalence ratio on the characteristics of lignite coal partial gasification products in fluidized bed. J Energy Inst 2025;119:102008. https://doi.org/10.1016/j.joei.2025.102008.

[30] Kresse G, Furthmüller J. Efficiency of ab-initio total energy calculations for metals and semiconductors using a plane-wave basis set. Comput Mater Sci 1996;6:15–50. https://doi.org/10.1016/0927-0256(96)00008-0.

[31] Kresse G, Furthmüller J. Efficient iterative schemes for ab initio total-energy calculations using a plane-wave basis set. Phys Rev B 1996;54:11169–86. https://doi.org/10.1103/PhysRevB.54.11169.

[32] Perdew JP, Burke K, Ernzerhof M. Generalized gradient approximation made simple. Phys Rev Lett 1996;77:3865–8. https://doi.org/10.1103/PhysRevLett.77.3865.

[33] Kresse G, Joubert D. From ultrasoft pseudopotentials to the projector augmented-wave method. Phys Rev B 1999;59:1758–75. https://doi.org/10.1103/PhysRevB.59.1758.

[34] Blöchl PE. Projector augmented-wave method. Phys Rev B 1994;50:17953–79. https://doi.org/10.1103/PhysRevB.50.17953.

[35] Ye C, Wang Q, Yu L, Luo Z, Cen K. Characteristics of coal partial gasification experiments on a circulating fluidized bed reactor under CO2O2 atmosphere. Appl Therm Eng 2018;130:814–21. https://doi.org/10.1016/j.applthermaleng.2017.11.071.

[36] Fast pyrolysis of corn stovers with ceramic ball heat carriers in a novel dual concentric rotary cylinder reactor. Bioresour Technol 2018;263:467–74. https://doi.org/10.1016/j.biortech.2018.05.033.

[37] Li X, Li B, Fu D, Feng J, Li W. The interaction between the char solid heat carrier and the volatiles during low-rank coal pyrolysis. J Anal Appl Pyrolysis 2018;136:160–8. https://doi.org/10.1016/j.jaap.2018.10.009.

[38] Pan D, Qu X, Bi J. Effect of gasified semi-coke on coal pyrolysis in the poly-generation of CFB gasification combined with coal pyrolysis. J Anal Appl Pyrolysis 2017;127:461–7. https://doi.org/10.1016/j.jaap.2017.06.028.

[39] Yu J, Lucas JA, Wall TF. Formation of the structure of chars during devolatilization of pulverized coal and its thermoproperties: a review. Prog Energy Combust Sci 2007;33:135–70. https://doi.org/10.1016/j.pecs.2006.07.003.

[40] Yildiz G, Ronsse F, Venderbosch R, Duren R van, Kersten SRA, Prins W. Effect of biomass ash in catalytic fast pyrolysis of pine wood. Appl Catal B Environ 2015;168–169:203–11. https://doi.org/10.1016/j.apcatb.2014.12.044.

[41] Calderón LA, Chamorro E, Espinal JF. Understanding the kinetics of carbon-hydrogen reaction: insights from reaction mechanisms on zigzag edges for homogeneous and heterogeneous formation of methane. Carbon 2017;118:597–606. https://doi.org/10.1016/j.carbon.2017.03.097.

[42] Ellison C, Abdelsayed V, Smith M, Shekhawat D. Comparative evaluation of microwave and conventional gasification of different coal types: experimental reaction studies. Fuel 2022;321:124055. https://doi.org/10.1016/j.fuel.2022.124055.

[43] Xu T, Chen J, Wu Y, Gao X, Bhattacharya S. Syngas production from two-step CO2 gasification of low rank coal in an entrained flow reactor. J Energy Inst 2022;103:169–76. https://doi.org/10.1016/j.joei.2022.06.004.

[44] Chareonpanich M, Zhang Z-G, Nishijima A, Tomita A. Effect of catalysts on yields of monocyclic aromatic hydrocarbons in hydrocracking of coal volatile matter. Fuel 1995;74:1636–40. https://doi.org/10.1016/0016-2361(95)00147-W.

[45] Wang Y, Li Y, Wang G, Wu Y, Yang H, Jin L, et al. Effect of Fe components in red mud on catalytic pyrolysis of low rank coal. J Energy Inst 2022;100:1–9. https://doi.org/10.1016/j.joei.2021.10.005.

[46] Cheng Y, Wang G, Wang Y, Ban Y, Li Y, Li Y, et al. Effect of red mud additive on the combustion performance of lignite and sulfur fixation behaviors. Energy Sources, Part A Recovery, Util Environ Eff 2023;45:7068–87. https://doi.org/10.1080/15567036.2023.2219646.

[47] Cahyono RB, bin Mansor M, Nomura T, Hidayat M, Budiman A, Akiyama T. Steam reforming of tar using low-grade iron ore for hydrogen production. Energy Fuels 2019;33:1296–301. https://doi.org/10.1021/acs.energyfuels.8b04122.

[48] Zhang B, Tian Z, Wang Q, Ma D, Jia R, Xie G, et al. Assessment of the impact of pyrolysis conditions on char reactivity through orthogonal experimental-based grey relational analysis. J Anal Appl Pyrolysis 2024;179:106426. https://doi.org/10.1016/j.jaap.2024.106426.

[49] Üstüntağ S, Şenyiğit E, Mezarcıöz S, Türksoy HG. Optimization of coating process conditions for denim fabrics by Taguchi method and grey relational analysis. J Nat Fibers 2022;19:685–99. https://doi.org/10.1080/15440478.2020.1758866.

[50] Microstructural evolution of coal to char after pyrolysis using laser-induced breakdown spectroscopy and Raman spectroscopy. Energy 2023;267:126558. https://doi.org/10.1016/j.energy.2022.126558.

[51] Tay H-L, Kajitani S, Zhang S, Li C-Z. Effects of gasifying agent on the evolution of char structure during the gasification of Victorian brown coal. Fuel 2013;103:22–8. https://doi.org/10.1016/j.fuel.2011.02.044.

[52] Zhang S, Hayashi J, Li C-Z. Volatilisation and catalytic effects of alkali and alkaline earth metallic species during the pyrolysis and gasification of Victorian brown coal. Part IX. Effects of volatile-char interactions on char–H2O and char–O2 reactivities. Fuel 2011;90:1655–61.

[53] Wang Z, Zhang L, Zhao Y, Feng S, Ma J, Kong W, et al. Experimental investigation on the evolution characteristics of anthracite-N and semi-coke reactivity under various O2/H2O pre-oxidation atmospheres. Fuel Process Technol 2021;216:106725. https://doi.org/10.1016/j.fuproc.2021.106725.

[54] Li X, Hayashi J, Li C-Z. FT-Raman spectroscopic study of the evolution of char structure during the pyrolysis of a Victorian brown coal. Fuel 2006;85:1700–7. https://doi.org/10.1016/j.fuel.2006.03.008.

[55] Williams RT, Bridges JW. Fluorescence of solutions: a review. J Clin Pathol 1964;17:371–94.

[56] Xu J, Su S, Sun Z, Qing M, Xiong Z, Wang Y, et al. Effects of steam and CO2 on the characteristics of chars during devolatilization in oxy-steam combustion process. Appl Energy 2016;182:20–8. https://doi.org/10.1016/j.apenergy.2016.08.121.

[57] Qing M, Su S, Chi H, Xu J, Sun Z, Gao J, et al. Relationships between structural features and reactivities of coal-chars prepared in CO2 and H2O atmospheres. Fuel 2019;258:116087. https://doi.org/10.1016/j.fuel.2019.116087.

[58] Tay H-L, Kajitani S, Zhang S, Li C-Z. Inhibiting and other effects of hydrogen during gasification: further insights from FT-Raman spectroscopy. Fuel 2014;116:1–6. https://doi.org/10.1016/j.fuel.2013.07.066.

[59] Zi-Zhao D, Zhang S, Qiang L, Ming-Hui D, Rui G, Jie-Ping W, et al. Boudouard reaction accompanied by graphitization of wrinkled carbon layers in coke gasification: a theoretical insight into the classical understanding. Fuel 2021;297:120747. https://doi.org/10.1016/j.fuel.2021.120747.

[60] Guo J, Shen Y, Wang M, Xie W, Kong J, Chang L, et al. Impact of chemical structure of coal on coke quality produced by coals in the similar category. J Anal Appl Pyrolysis 2022;162:105432. https://doi.org/10.1016/j.jaap.2022.105432.

[61] Pope CG. X-Ray diffraction and the bragg equation. J Chem Educ 1997;74:129. https://doi.org/10.1021/ed074p129.

[62] Holzwarth U, Gibson N. The Scherrer equation versus the "Debye-Scherrer equation.". Nat Nanotechnol 2011;6:534. https://doi.org/10.1038/nnano.2011.145. 534.

[63] Xu M, Wu Y, Nan D, Lu Q, Yang Y. Effects of gaseous agents on the evolution of char physical and chemical structures during biomass gasification. Bioresour Technol 2019;292:121994. https://doi.org/10.1016/j.biortech.2019.121994.
[64] Lee S, Choi J, Chung YS, Kim J, Moon S, Lee S. Understanding the catalytic mechanism of calcium compounds for enhancing crystallinity in carbon fiber. Chem Eng J 2024;479:147728. https://doi.org/10.1016/j.cej.2023.147728.
[65] Zhao Y, Xing C, Shao C, Chen G, Sun S, Chen G, et al. Impacts of intrinsic alkali and alkaline earth metals on chemical structure of low-rank coal char: Semi-quantitative results based on FT-IR structure parameters. Fuel 2020;278:118229. https://doi.org/10.1016/j.fuel.2020.118229.
[66] Ge L, Zhang Y, Wang Z, Zhou J, Cen K. Effects of microwave irradiation treatment on physicochemical characteristics of Chinese low-rank coals. Energy Convers Manag 2013;71:84–91. https://doi.org/10.1016/j.enconman.2013.03.021.
[67] Zhu Y, Tian F, Liu Y, Cui L, Dan Y, Du C, et al. Comparison of the composition and structure for coal-derived and petroleum heavy subfraction by an improved separation method. Fuel 2021;292:120362. https://doi.org/10.1016/j.fuel.2021.120362.
[68] Wang B, Sun L, Su S, Xiang J, Hu S, Fei H. Char structural evolution during pyrolysis and its influence on combustion reactivity in air and oxy-fuel conditions. Energy Fuels 2012;26:1565–74. https://doi.org/10.1021/ef201723q.
[69] Chen Y, Yin H, He D, Gong H, Liu Z, Liu Y, et al. Low temperature oxidized coke of the ultra-heavy oil during in-situ combustion process: structural characterization and evolution elucidation. Fuel 2022;313:122676. https://doi.org/10.1016/j.fuel.2021.122676.
[70] Li Y, Feng D, Sun S, Zhao Y, Shang Q, Chen K, et al. Biomass-coal reburning: competitive mechanism of gas-solid product activation coal char. Energy 2022;261:125225. https://doi.org/10.1016/j.energy.2022.125225.
[71] Tian Z, Zhang B, Wang Q, Jia R, Ma D, Xie G. Evaluation of the influence of different conditions on the Na/Cl release and characteristics of high-alkali coal pyrolysis products by orthogonal and single-factor experiments. Fuel 2025;391:134602. https://doi.org/10.1016/j.fuel.2025.134602.
[72] Peng F, Lu Y, Wang Y, Yang L, Yang Z, Li H. Predicting the formation of disinfection by-products using multiple linear and machine learning regression. J Environ Chem Eng 2023;11:110612. https://doi.org/10.1016/j.jece.2023.110612.
[73] Khan MR. Significance of char active surface area for appraising the reactivity of low- and high-temperature chars. Fuel 1987;66:1626–34. https://doi.org/10.1016/0016-2361(87)90353-X.
[74] Liu M, Bai J, Kong L, Bai Z, He C, Li W. The correlation between coal char structure and reactivity at rapid heating condition in TGA and heating stage microscope. Fuel 2020;260:116318. https://doi.org/10.1016/j.fuel.2019.116318.
[75] Roberts MJ, Everson RC, Domazetis G, Neomagus HWJP, Jones JM, Van Sittert CGCE, et al. Density functional theory molecular modelling and experimental particle kinetics for CO2–char gasification. Carbon 2015;93:295–314. https://doi.org/10.1016/j.carbon.2015.05.053.
[76] Wang Y, Hu X, Mourant D, Song Y, Zhang L, Lievens C, et al. Evolution of aromatic structures during the reforming of bio-oil: importance of the interactions among bio-oil components. Fuel 2013;111:805–12. https://doi.org/10.1016/j.fuel.2013.03.072.
[77] Bai R, Liu L, Li N, Liu Q, Meng Y, Teng Y, et al. Insight into coal catalytic gasification mechanism of Na or Ca using experiments combined with DFT calculations with carbon black as a novel coal model. Fuel 2023;349:128654. https://doi.org/10.1016/j.fuel.2023.128654.
[78] Montoya A, Mondragón F, Truong TN. First-Principles kinetics of CO desorption from oxygen species on carbonaceous surface. J Phys Chem A 2002;106:4236–9. https://doi.org/10.1021/jp0144294.
[79] Chen N, Yang RT. Ab initio molecular orbital study of the unified mechanism and pathways for gas−carbon reactions. J Phys Chem A 1998;102:6348–56. https://doi.org/10.1021/jp981518g.
[80] Dzade NY, Roldan A, De Leeuw NH. A density functional theory study of the adsorption of benzene on Hematite (α-Fe2O3) surfaces. Minerals 2014;4:89–115. https://doi.org/10.3390/min4010089.
[81] Treu P, Gonçalves D, Nilayam ARL, Grunwaldt J-D, Saraçi E. One-Pot Cascade reaction from epoxide to carboxylic acids using bifunctional Fe-ZSM-5 n.d. https://doi.org/10.1002/cctc.202400626.